FACULTY OF PHYSICS AND ASTRONOMY

UNIVERSITY OF HEIDELBERG

State Examination Thesis

in Physics

submitted by

Holger Eric Jörg

born in Schwetzingen, Germany

2012

Commissioning of a Prototype Transition Radiation Detector Chamber (ALICE)

This state examination thesis has been carried out by
Holger Eric Jörg
at the Physikalisches Institut Heidelberg
under the supervision of
Dr. Kai Schweda

Commissioning of a Prototype Transition Radiation Detector Chamber (ALICE)

ALICE (A Large Ion Collider Experiment) at the Large Hadron Collider at CERN, Geneva, comprises a series of detectors. A prototype chamber of one of these detectors, a Transition Radiation Detector (TRD), has been commissioned within this thesis project. Cosmic particles were used for the commissioning. A trigger set-up, which consists of scintillator assemblies and photomultipliers, provides the necessary trigger for the TRD. A read-out system of TRD data has been set up. It consists of an MCM (Multi Chip Module) and a USB adapter for the communication between trigger, MCM and a computer. The USB adapter has been developed within this thesis. TRD data is sent to the computer, where it is analysed. A real-time event and track display has been created. It is possible to observe particle tracks in the TRD on a computer in real-time. During the commissioning phase, several key measurements were performed and compared to values from the literature, i.e. drift velocities for different drift fields and electron attachment. The effect of a filter within the read-out chip, the tail cancellation filter, on the performance of the set-up has been examined.

Aufbau und Inbetriebnahme einer Prototypenauslesekammer des Übergangsstrahlendetektors des ALICE

ALICE (A Large Ion Collider Experiment) am Large Hadron Collider am CERN, Genf, besteht aus einer Reihe von Detektoren. Eine Prototypenkammer einer dieser Detektoren, ein Übergangsstrahlendetektor (TRD), wurde während dieser Abschlussarbeit in Betrieb genommen. Dafür wurde kosmische Strahlung als Teilchenquelle verwendet. Ein Trigger, bestehend aus Szintillatoren und Photomultipliern, liefert den notwendigen Trigger für die TRD Kammer. Ein Auslesesystem für die Daten des TRDs wurde aufgebaut. Es besteht aus einem MCM (Multi Chip Module) und einem USB-Adapter, welcher für die Kommunikation zwischen Trigger, MCM und Computer verantwortlich ist. Der USB-Adapter wurde während dieser Abschlussarbeit entwickelt. TRD Daten werden zu einem Computer gesendet, wo diese analysiert werden. Ein Display, welches in Echtzeit Ereignisse und Teilchenspuren in der TRD Kammer darstellt, wurde entwickelt. Es ist möglich Teilchenspuren im TRD auf einem Computer in Echtzeit zu betrachten. Während der Inbetriebnahme wurden einige zentrale Messungen vorgenommen und die Ergebnisse mit Literaturwerten verglichen. Es wurden zum Beispiel Driftgeschwindikeiten für verschiedene Driftfelder und Elektron Attachment gemessen. Der Effekt eines Filters im Auslesechip, der den Signalschwanz unterdrückt, auf die Betriebseigenschaften des Aufbaus wurde untersucht.

Contents

List of Figures

1. Introduction

The composition of matter has been a rewarding topic of scientific research ever since ancient times. Models explaining the nature of matter have been presented by natural scientists and philosophers. The idea that matter consists of discrete building blocks, elementary and indivisible particles, was first forwarded by the Greek philosopher Leucippus and Demokrit, who lived in the 5th century BC. Today the Standard Model of Particle Physics (SM), explains the basic constituents of matter and the interactions between these constituents. The basic constituents, the elementary particles, are quarks (u, d; c, s; t, b) and leptons ($e^{\pm}$; $\mu^{\pm}$; $\tau^{\pm}$), which are both arranged in three families. Three of the four fundamental interactions are included in the SM. There are twelve vector bosons mediating these three interactions. The electromagnetic interaction is mediated by the photon (γ), the weak interaction by $W^{\pm}$ - bosons and the Z^0 - boson, and the strong interaction by eight gluons (g). Gravitation, the fourth fundamental interaction is not included in the SM. Quantum Electrodynamics (QED), the relativistic quantum field theory of electrodynamics, describes the interaction of particles under the electrodynamic interaction. QED was used as a paradigm for other Quantum Field Theories, as e.g. Quantum Chromodynamics (QCD). QCD describes the interaction of colour-charged particles, quarks and gluons, under the strong interaction. It is the basis of nuclear force. Gluons, in comparison to photons, carry charge themselves. Free colour-charged particles have not been observed in experiments, yet. This is interpreted as confinement of colour-charged objects in hadrons. At high enough energy densities, this confinement is suspended, and a state called the Quark Gluon Plasma (QGP) is formed: matter undergoes a phase transition from hadronic to partonic matter, in which colour-charged particles are unbound.

The Large Hadron Collider (LHC) at CERN in Geneva hosts an experiment dedicated to study the formation and properties of the QGP: ALICE (A Large Ion Collider Experiment). Two beams of nuclei, lead ions, are collided at ultra-relativistic energies. The energy density at the interaction point is high enough to form the QGP. The properties of the QGP are analysed by reconstructing the trajectories and properties of particles produced in the initial plasmonic state. ALICE consists of several particle detectors arranged around the interaction point. These detectors provide information on particle trajectories as well as particle identification. One of these detectors is the Transition Radiation Detector (TRD). It provides electron identification, tracking capabilities and a fast trigger. Prototype TRD chambers were constructed to test their performance. This thesis project deals with the commissioning of such a prototype TRD chamber.

This thesis is organised as follows. Chapter 2 gives a brief summary of the interaction of particles with matter relevant for this thesis project. Chapter 3 contains an introduction to the experimental environment: CERN, the LHC, and ALICE are introduced. Chapter 4 focusses on the principle of operation of the ALICE TRD. Chapter 5 contains information on the particles used in the commissioning of the TRD chamber, cosmic radiation. For the data acquisition, TRD chambers need an external signal, a trigger. Chapter 6 describes the set-up of a trigger for cosmic particles. Chapter 7 describes the actual commissioning of the TRD chamber: the chamber is supplied with gas and high

1

voltage. Chapter 8 contains information on the read-out system used for the prototype TRD chamber. The data acquisition and tracking algorithm are addressed, as well as the the online display. A performance measurement, a measurement of average pulse height distributions, has been carried out. Chapter 9 contains its results as well as a comparison to literature data. A conclusion and outlook are presented in chapter 10.

2. Interactions of Particles with Matter

Particle detectors make use of the interactions of particles with matter. Particles with different properties, e.g. electrically charged in comparison to neutral particles, interact with different media, e.g. solids, fluids, or gases, in different ways, e.g. they ionise the atoms the medium consists of. To construct a detector, it is therefore necessary to keep in mind which particles at which velocities, energies and momenta are supposed to be detected. The function of the ALICE TRD, for example, is to distinguish between electrons and pions; in some respect, the interaction of electrons and pions in the detector material has to differ, making it possible to distinguish between signals coming from electrons and pions. Such complex detectors, as for example the ALICE detector, face another challenge. The ALICE subdetectors are arranged like an onion shell around the beam axis and interaction point. Particles traverse a series of detectors on their way from the interaction point to the detectors located further away from the interaction point. Thus energy losses of particles in detector material closer to the interaction point can lead to signal losses in detectors further away from the interaction point. The range of possible interactions of particles with matter is too vast to be presented in such a thesis. To keep this theoretical introduction to interactions of particles with matter as brief as possible, only those interactions are addressed here that are relevant for the particle detectors and phenomena used in this thesis project.

2.1. Interactions of Charged Particles with Matter

The interaction of charged particles with matter is dominated by the electromagnetic interaction. A number of possible processes can occur when a charged particle traverses a material: excitation and ionisation of the atoms within the material, as well as radiative processes, like Bremsstrahlung, emission of Cherenkov Radiation, and, in heterogene media, Transition Radiation [8]. For the purposes of this experiment, Cherenkov Radiation is not relevant; the discussion focusses instead on excitation and ionisation, Bremsstrahlung, as well as Transition Radiation.

2.1.1. Excitation and Ionisation

For a particle with a velocity of $\beta = v/c$ transversing a medium, the Bethe-Bloch formula approximately describes the energy loss of the particle through excitation and ionisation of the medium. It is only valid for velocities in the region of $0.1 \leq \beta\gamma \leq 1000$, corresponding to energies of a few MeV to around 100 GeV [7]. These velocity and energy regions are the ones interesting for the experiment conducted in this thesis project. Above an energy of 100 GeV, radiative processes, e.g. pair production, become more important than ionisation in understanding the particle energy loss. The average energy loss per unit length $-\left\langle \frac{dE}{dx} \right\rangle$ due to ionisation is given by the Bethe-Bloch formula [9]:

$$-\left\langle \frac{dE}{dx} \right\rangle = 4\pi r_e^2 m_e c^2 N_a z^2 \frac{Z}{A} \frac{1}{\beta^2} \left(\frac{1}{2} \ln \left(\frac{2m_e c^2 \beta^2 \gamma^2 T_{max}}{I^2} \right) - \beta^2 - \frac{\delta(\beta\gamma)}{2} \right) \qquad (2.1)$$
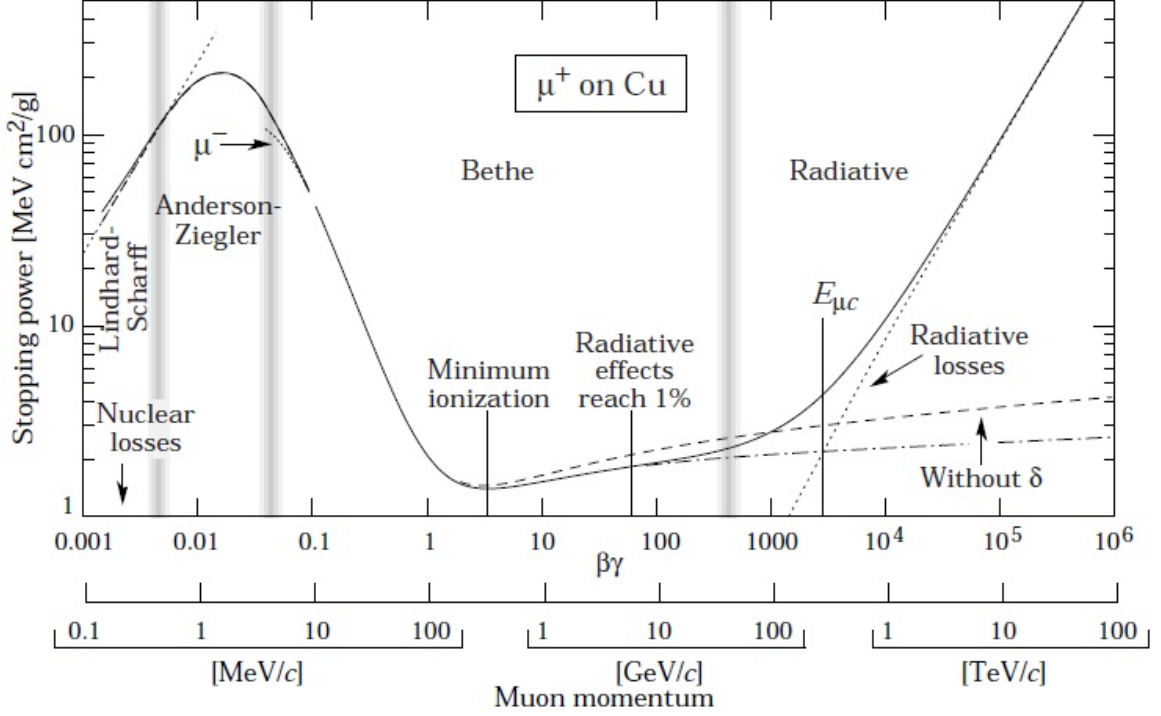
Figure 2.1: Stopping power (mean rate of energy loss $-\langle\frac{dE}{dx}\rangle$) for positive muons in copper as a function of $\beta\gamma$ over nine order of magnitude in momentum. Solid lines represent the total stopping power. This figure has been taken from [9]

Here, N_A is the Avogadro constant, r_e and m_e are the classical electron radius and electron mass, Z and A are atomic and mass numbers of the medium, and I is the effective ionisation potential of the medium. T_{max} is the maximum kinetic energy which can be imparted to a free electron in a single collision [9]. $\delta(\beta\gamma)$ is the density effect correction to ionisation energy loss. z describes the charge of the particle in units of e. A more detailed explanation of the parameters in Equ. 2.1 as well as its derivation, can be found in [7] [8]. An important fact for this experiment is that the energy loss of the particle through ionisation and excitation $-\langle\frac{dE}{dx}\rangle$ does not depend on the mass of the ionising particle; it only depends on its velocity and charge.

Fig. 2.1 shows the mean energy loss of positive muons in copper as a function of the momentum of muons. In the energy region described by the Bethe-Bloch equation, the energy loss first decreases as a function of β^{-2}, then there is a broad minimum around $\beta\gamma \simeq 4$. Particles with velocities corresponding to this minimum, usually around $3 \leq \beta\gamma \leq 4$, are called minimum ionising particles. For higher velocities, the term β^{-2} becomes nearly constant. The energy loss is dominated by the logarithmic term in Equ. 2.1 [7]. This is due to relativistic effects: the electric field flattens and extends. For even higher particle velocities ($\beta\gamma \simeq 1000$), radiative losses dominate and the Bethe-

Bloch equation is not valid any longer.

2.1.2. Bremsstrahlung

Charged particles also radiate energy in media through radiative processes, as e.g. Bremsstrahlung. For highly relativistic particles ($\beta \simeq 1$) these losses dominate. If a charged particle is accelerated in the Coulomb field of a nucleus, a fraction of its kinetic energy is emitted as photons. The energy loss of charged particles by Bremsstrahlung can be described by the following equation [7]:

$$-\left\langle \frac{dE}{dx} \right\rangle = 4\alpha N_a \frac{Z^2}{A} z^2 \left(\frac{1}{4\pi\epsilon_0} \frac{e^2}{mc^2} \right)^2 E \ln\left(\frac{183}{Z^{1/3}} \right) \tag{2.2}$$

Z, A are the atomic and mass number of the medium; z, E and m are, respectively, the charge, energy and mass of the incoming particle. The energy loss via Bremsstrahlung is thus proportional to the charge and energy of the incoming particle, as well as inversely dependent on its squared mass. For light particles with a low atomic number, e.g. electrons, the energy loss via Bremstrahlung is more significant than for heavy particles. For electrons the energy loss through Bremsstrahlung becomes higher than the energy loss through ionisation at energies above $E_c \sim 580 \frac{MeV}{Z}$[11]. Commonly the concept of a radiation length X_0 is used for energy losses through radiative processes in media. It is defined as the length, after which the energy of a particle has decreased to 1/e of its initial energy due to Bremsstrahlung radiation. For electrons Equ. 2.2 can be written as:

$$-\frac{dE}{dx} = \frac{E}{X_0}; \quad \frac{1}{X_0} = \frac{4\alpha N_A Z^2 r_e^2 \ln\left(\frac{183}{Z^{-1/3}} \right)}{A} (cm^2/g) \tag{2.3}$$

In this experiment, energy losses of highly relativistic particles through radiative processes becomes relevant when the interaction of cosmic particles with the Earth's atmosphere is examined.

2.1.3. Transition Radiation

Transition radiation is produced when a highly relativistic charged particle traverses the boundary between media with different dielectric properties [7]. A detailed explanation of the production of transition radiation and the energy charged particles deposit through this process would be based on the energy transfer via virtual photons between the
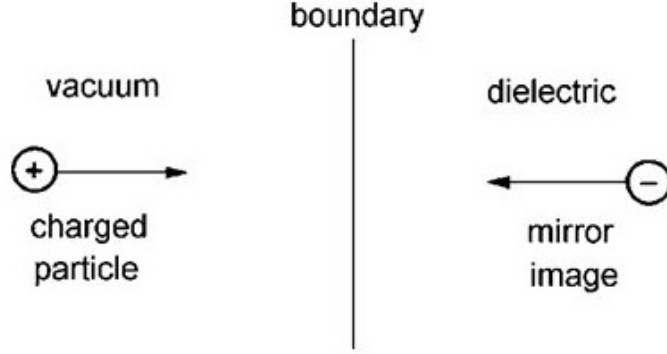
Figure 2.2: Illustration of the production of transition radiation at boundaries [7]

incoming particle and the medium [8]. The production of transition radiation can also be illustrated with the model of mirror charges, as shown in Fig. 2.2 :

The incoming particle moves towards a boundary between two media of different dielectric properties, in this case a boundary between vacuum and an arbitrary dielectric. Together with its mirror charge, it forms an electric dipole. As the particle is moving towards the boundary, the field strength becomes smaller and finally vanishes when the particle traverses the boundary. The time-dependent electric field strength leads to an emission of photons, i.e. electromagnetic transistion radiation [7]. The number of emitted photons N_γ with energy $\hbar\omega$ above a fixed energy $\hbar\omega_0$ is [9]:

$$N_\gamma(\hbar\omega > \hbar\omega_0) = \frac{\alpha z^2}{\pi} \left[\left(\ln\left(\frac{\gamma \hbar \omega_P}{\hbar\omega_0}\right) - 1 \right)^2 + \frac{\pi^2}{12} \right] \qquad (2.4)$$

where

$$\hbar\omega_P = \sqrt{4\pi N_e r_e^3} \frac{m_e c^2}{\alpha} \qquad (2.5)$$

where ω_P is the plasma frequency of the medium. The number of photons, which are emitted above a fixed energy $\hbar\omega_0$ of the incoming particle, grows as a function of $(ln\gamma)^2$) Thus, the number of emitted photons depends on the Lorentz factor of the particle γ. At the boundary the emission probability of a transition radiation photon is of the order of $\alpha = \frac{1}{137}$ [7]; many such boundaries are needed to have a sufficiently high number of photons to be used for particle detection. With a periodical arrangement of boundaries, the interferences of transition radiation photons emitted at the separate boundaries create a threshold behaviour at $\gamma \simeq 1000$ [7]. Transition radiation photons are emitted in an angle of

$$\theta = \frac{1}{\gamma_{particle}}. \tag{2.6}$$

For highly relativistic particles, $\gamma\beta > 1000$, this means that most photons are emitted in the particle's direction of flight. For particles with such velocities, the emitted photons have energies in the soft x-ray region, $2 \text{ keV} \leq \text{E} \leq 40 \text{ keV}$.

To sum up the information on transition radiation, transition radiation photons are emitted at boundaries of media with different dielectric properties. The number of emitted photons depends on the particle's Lorentz factor with a threshold behaviour at $\gamma \simeq 1000$. The small yield of transition radiation photons at single boundaries makes it necessary to have a high number of boundaries. Transition radiation is predominantly emitted in the particle's direction of flight. For particles with $\gamma\beta \simeq 1000$, the emitted photon energy is in the x-ray region. All of these characteristics of transition radiation are relevant for the construction of transition radiation detectors.

2.2. Interactions of Photons - Photoelectric Effect

In the photoelectric effect, photons are absorbed by atomic electrons. If the energy of the photon is larger than the binding energy of the atomic electron, the electron is emitted and the atom is ionised. The photoelectric effect is only possible for atomic electrons and not for free electrons; the atomic nucleus, with its high mass, takes the recoil momentum. The photoelectric cross section is given in the Born approximation by [7]:

$$\sigma_{photo}^{K} = (\frac{32}{\varepsilon^7})^{1/2} \alpha^4 Z^5 \sigma_{Th}^{e} \tag{2.7}$$

where $\epsilon = E_\gamma / m_e c^2$ is the reduced photon energy and $\sigma_{Th}^{e} = \frac{8}{3}\pi r_e^2 = 6.65 \cdot 10^{-25} \text{ cm}^2$ is the Thomson cross section for elastic scattering of photons on electrons. The photoelectric cross section depends strongly on the atomic number of the absorbing medium and on the reduced energy of the photon.

3. Experimental Environment: CERN and the LHC

CERN (*Conseil Europen pour la Recherche Nuclaire*) is the European Organisation for Nuclear Research. Cern was founded in 1954. Based in Geneva, Swizerland, on the Franco-Swiss border, the site provides infrastructure and laboratories for experiments dedicated to high energy physics. It houses the Large Hadron Collider (LHC), a particle accelerator capable of accelerating opposing hadron beams up to $\sqrt{s} = 8$ TeV. The experiments conducted at CERN address such fundamental issues as the following: underlying structure of matter and fundamental interactions between elementary particles. It also houses an experiment solely dedicated to heavy-ion physics: A Large Ion Collider Experiment (ALICE). Significant scientific achievements made in particle physics at CERN are the following: the discovery of neutral currents in the Gargamelle bubble chamber in 1973; the discovery of the W^+, W^- and Z^0 bosons in 1983; the creation of antihydrogen in 1995; the experimental proof of direct CP violation in 1999; and most recently, the discovery of a scalar boson a mass between 125 GeV and 126 GeV, a candidate for the long-sought after Higgs boson.

3.1. The Large Hadron Collider

The Large Hadron Collider, began operation at CERN on 10th September 2008. The first collision of protons at the LHC occurred on 30th March 2010. The LHC accelerates opposing hadron beams, protons and lead ions, up to 99.999999 % of the speed of light. Proton beams are collided at a centre-of-mass energy of $\sqrt{s} = 8$ TeV while lead ions are collided at centre-of-mass energies of $\sqrt{s} = 2.76$ TeV per particle. The LHC was designed to have collision rates of 40 MHz for protons and 8 MHz for lead nuclei. Such collision rates lead to instantaneous luminosities of 10^{34} cm^{-2}s^{-1} and $5 \cdot 10^{26}$ cm^{-2}s^{-1}, respectively. The high centre-of-mass energies and luminosities make it possible to study processes with low cross-sections while maintaining moderate event rates. The hadron beams are collided at four interaction points. At each of the four, particle detectors are used to study collision products. Fig. 3.1 shows a schematic representation of the CERN facility, the different pre-accelerators for the LHC and the four major experiments: ATLAS (A Toroidal LHC ApparatuS), LHCb (Large Hadron Collider Beauty), CMS (Compact Muon Solenoid) and ALICE (A Large Ion Collider Experiment).

The four major experiments at the LHC are realised by particle detectors at the four interaction points. While the detectors are of different design, each comprising several subdetectors in a particular order around the interaction point, they all follow the same overall principle. Particles produced in the collisions are detected. The aim is to reconstruct the trajectories of the emerging particles within a magnetic field to study their properties. The reconstruction of tracks of particles produced in the collision enables us to draw conclusions about the processes taking place during the collision. What follows is a brief description of the four major experiments conducted at the LHC.
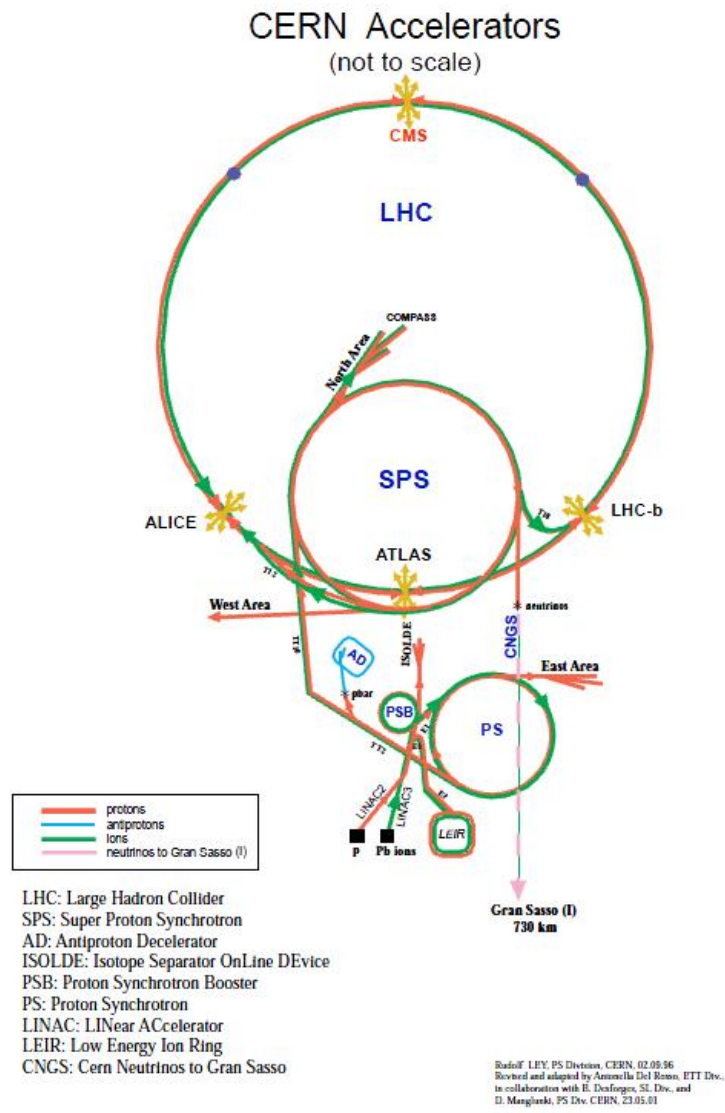
Figure 3.1: Schematic representation of the accelerator complex at CERN and different particle types accelerated at various accelerator sites [1]

ATLAS, A Toroidal LHC ApparatuS, is a general purpose experiment addressing a broad physics variety. The most prominent of these is the search for the Higgs boson through its decay channels. Other issues that are addressed are new physics phenomena like supersymmetry, extra dimensions or the search for dark matter candidates.

CMS, Compact Muon Solenoid, addresses similar issues as ATLAS. Using a detector system for muons, built around a superconducting solenoid which provides a magnetic field of 3.8 T, muons produced in the collision can be tracked efficiently in a broad momentum range.

The LHCb, Large Hadron Collider beauty, is a specialised B-meson experiment. By means of analysing the decay of B-mesons, the origin of CP violation is examined. CP asymmetry, leading to differences in decay modes of particles and their antiparticles, might be responsible for the matter-antimatter disbalance in our known universe.

ALICE, A Large Ion Collider Experiment, is the only experiment at CERN solely dedicated to heavy-ion physics. Its major goal is studying the properties of the Quark Gluon Plasma (QGP), a state of matter existing at high energy densities in which confinement of quarks is suspended. ALICE hosts the detector type of which a prototype is the subject of this thesis project, a Transition Radiation Detector.

3.2. ALICE: A Large Ion Collider Experiment

ALICE is the only experiment at the LHC solely dedicated to heavy-ion physics. The aim is to characterise the QGP: therefore two heavy ions, two lead nuclei, are collided at ultra-relativistic energies. The initial energy density and temperature is of the order of 1000 GeV/fm^3 and 1 GeV, respectively [2]. At such high energy densities confinement of quarks into colour-free hadrons is suspended, and a state called Quark Gluon Plasma is formed. In this formation, matter undergoes a phase transition from hadronic to partonic matter; quarks and gluons are unbound. In this state, multiple scattering among quark and gluon constituents occurs. In ALICE the products of this multiple scattering are studied. The objective is to study the formation and properties of the QGP.

The realisation of such an experiment faces the following challenge: the QGP is not directly observable; after a short life time, of the order of $10 \frac{fm}{c}$ [4], after its formation in collisions partonic matter freezes out, i.e. the energy density and temperature become smaller, and there is a phase transition back towards hadronic matter, in which quarks and gluons are confined in hadrons. To study the initial plasmonic state, particles produced in the initial plasmonic state are used as probes. Quarkonia are considered to be a sensitive probe of deconfinement [23]. One of these probes is the J/ψ meson, the bound state of a charm and anti charm quark. The J/ψ production depends on several mechanisms that are predicted to modify its production in the presence of QGP, e.g. suppression of its production rate because of colour screening. A study of the

J/ψ yield can give information on the properties of the medium created in heavy-ion collisions [3]. The J/ψ is unstable; it is measured through its dileptonic decay channel, $J/\psi \longrightarrow e^+e^-$. Well-reconstructed tracks of electrons and positrons are provided by the ALICE subdetectors. Thus by analysing the reconstructed tracks of particles produced in the collsion, conclusions about the properties of the QGP can be drawn.

The ALICE detector, as shown in Fig. 3.2, consists of a central barrel, placed in a homogeneous, axial magnetic field (B = 0.5 T), provided by the L3 magnet. Tracks of charged particles are bent; the radius of their curvatures depends on their momentum. To supply tracks of particles, and thus draw conclusion about their - kinematic - properties is the main function of the Time Projection Chamber (TPC), a gas-filled cylindrical chamber with multiwire proportional chambers as endplates. The TPC also provides particle identification. This gas-filled barrel detector has full azimuthal coverage and covers a pseudo-rapidity η range of ± 0.9 ($\eta = -ln(tan\frac{\theta}{2})$). The only detector closer to the interaction point is the Inner Tracking System (ITS), which consists of six layers of silicon detectors. The ITS provides tracking in the harsh environment near the interaction point. Attached to the TPC, there is the Transition Radiation Detector (TRD). This gas-filled detector provides electron identification as well as further tracking capabilities. The Time Of Flight detector (TOF) consists of multiresistive plate chambers covering an active area of 150 m^2. It provides π/K separation up to momenta of 2.2 GeV/c and K/p separation up to momenta of 4 GeV/c by precise time measurements with a resolution of 100 ps. There are further detectors, which do not cover the full azimuthal angle, as e.g. the Photon Spectrometer (PHOS), a high resolution electromagnetic calorimeter, which provides photon measurements. There is also a set of forward detectors and a muon arm. The forwards muon spectrometer records decays of heavy quarkonia in the $\mu^+\mu^-$-channels [5]. For further information on the ALICE subsystems consult the "ALICE Physics Performance Report" [5].
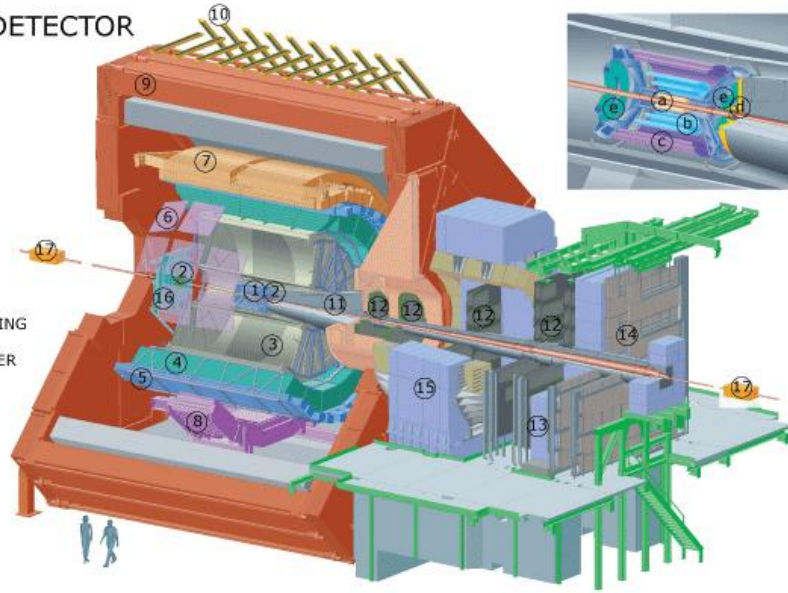
Figure 3.2: Schematic cross-section of the ALICE detector and its subsystems [5]

4. The ALICE Transition Radiation Detector

The ALICE Transition Radiation Detector (TRD) consists of 522 detector modules, which are segmented into 18 supermodules. Each supermodule holds up to 30 TRD modules, which are arranged into 5 stacks of 6 chambers each [2]. The 18 supermodules are supported by the space frame, shown in Fig. 4.1, the main support structure for many of the ALICE subdetectors.
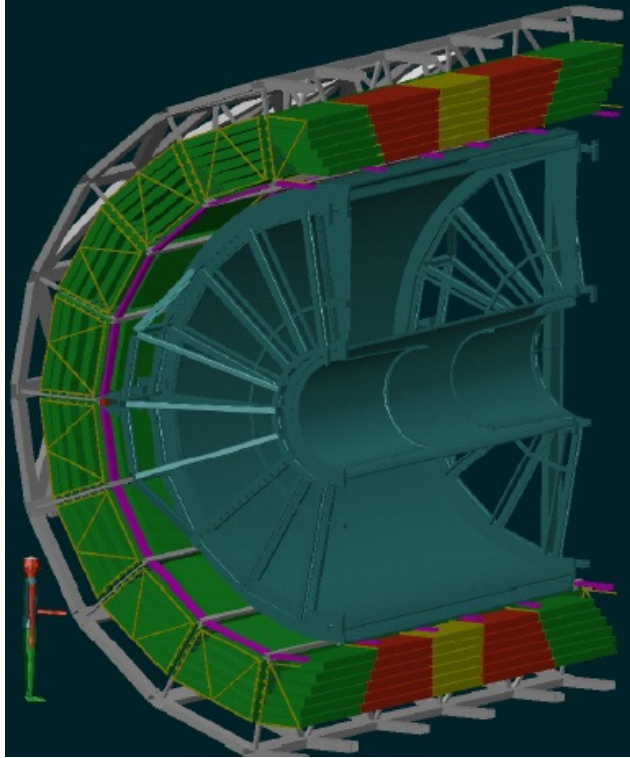
Figure 4.1: Schematic drawing of one half of the ALICE TRD. The 18 supermodules, consisting of 30 detector modules, are arranged around the beam axis covering a radius of 2945 mm to 3691 mm. Each supermodule consists of 5 stacks 6 modules [10]

The Transition Radiation Detector used in ALICE has three functions: tracking of particles passing through it, electron identification for particles with momenta above 1 GeV/c and providing trigger information based on tracks with available particle identification information. It consists of three parts, as illustrated in Fig. 4.2: a radiator, a readout chamber and front-end electronics. The radiator serves as an entry window for particles entering the TRD; depending on the Lorentz factor γ of the particles, transition radiation is produced. The second part is the readout chamber, a multiwire proportional chamber (MWPC) with a drift chamber and a read-out pad plane. The third part, the front-end electronics consists of a Multi-Chip Module (MCM), which is connected to the
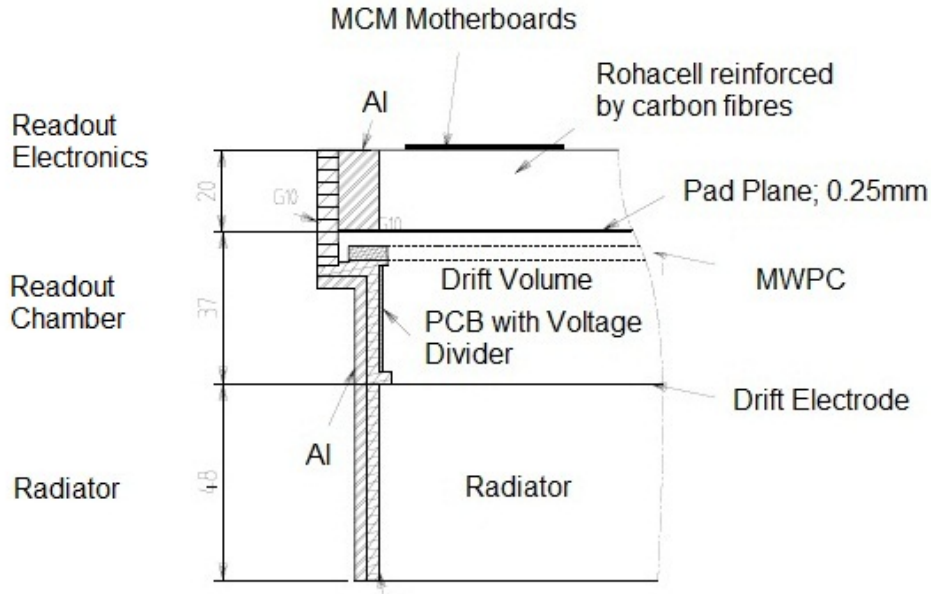
Figure 4.2: Cross section through a TRD chamber [6]

read-out pads. The TRD is filled with gas: a mixture of Xenon and Carbondioxide (85 - 15) [2]. Ionising particles produce charge clusters in the gas; these charge clusters drift towards the MWPC, where the charge signals are amplified. Additionally, for charged particles with a Lorentz factor of $\gamma >$1000, transition radiation photons are produced in the radiator. These photons are absorbed by the gas, thereby ionising it. Ionisation clusters due to transition radiation also drift towards the MWPC and are amplified there. Positive charges, which are produced in the amplification, induce analogue signals on the pads. The pads are connected to the front end electronics, where the signals are digitised and data is processed. Tracking as well as particle identification can be done by analysing the signals induced on the pads. Processed data is sent to the Global Tracking Unit (GTU), where possible tracks are calculated. The tracks contribute to the trigger decision of the Central Trigger Processor (CTP).

4.1. Radiator

From a physic point of view, the requirements of the ALICE TRD radiator are the following: the highest possible production rate of TR photons for charged particles with $\gamma >$1000 and a low absorption of these photons. For these purposes, usually stacks of polypropylene foils are used. For the TRD radiator at ALICE, there are also mechanical constraints: within the detector there has to be as little dead material as possible to minimize radiation losses [2]. A special support structure for the radiator is therefore impossible to realise. The radiator has to support itself and furthermore provide support for the rest of the TRD structure. Foils do not meet these requirements, while
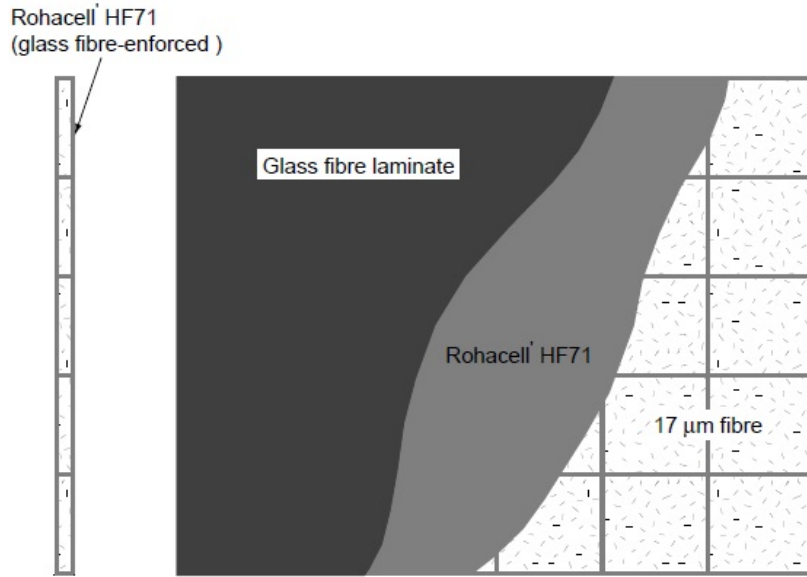
Figure 4.3: The principal design of the TRD sandwich radiator [2]

a construction of polypropylene fibres and polymethacrylimide (PMI) foam, Rohacell HF71 foam, illustrated in Fig. 4.3, does. It has a sufficiently high production rate of TR photons, a low absorption of these, as well as enough mechanical stability to serve as a support structure. The final design of the TRD radiator consists of two plates of Rohacell HF71 foam, supported by glass fibre laminate, which surround the main radiator material, the ploypropylene fibres. The radiator has a thickness of 48mm.

Electron identification and pion rejection are one of the main functions of the TRD. Electrons passing through the TRD leave a distinct signal due to their production of transition radiation in the TRD radiator. The production of transition radiation shows a threshold behaviour: charged particles with a Lorentz factor of γ >1000 produce transition radiation photons at boundaries of media with different dielectric properties. The ploypropylene fibres, the main radiator material, supply many such boundaries. Electrons, with their mass of $m_e = 0.511$ MeV/c^2, produce transition radiation if their momentum is larger than $p_e \approx 0.5$ GeV/c. Pions, with their mass of $m_\pi = 139.6\ MeV/c^2$, only produce transition radiation if their momentum is larger than $p_\pi \approx 140$ GeV/c. For momenta of a few GeV/c, the signals electrons and pions produce while transversing the TRD are different: electrons produce transition radiation photons, which enter the readout chamber of the TRD. Thus the threshold behaviour of transition radiation makes electron identification and thus a pion rejection possible.
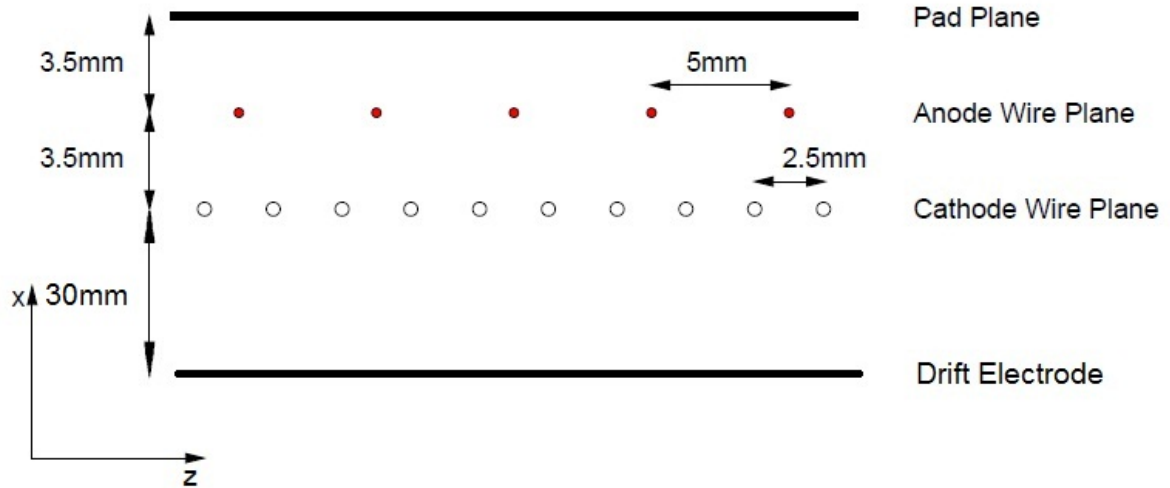
Figure 4.4: Wire geometry of the ALICE TRD read-out chamber (adapted from [2])

4.2. Read-Out Chamber

The ALICE TRD read-out chamber consists of a drift chamber, a multi wire proportional chamber (MWPC) and a pad plane. The read-out chamber is filled with gas. Charged particles, which pass through the chamber ionise the gas. The gas also enables high drift velocities of the ionisation clusters and a high amplification of these. The drift region, with a length of 30 mm, is separated from the multi wire proportional chamber by a cathode wire plane, as shown in Fig. 4.4. The drift electrode at the beginning of the drift region is put on negative potential (-2.1 kV). The anode wires in the MWPC are put on positive potential (+1.53 kV). The drift electrode is a mylar foil with a thickness of 50 μm. It serves as an entry window for particles. When an ionising particle passes through the gas-filled detector, electrons and positive ions are produced. For the gas mixture used in the ALICE TRD, a minimum ionising particle produces approximately 275 e^-/cm. In addition to that, particles with a Lorentz factor of $\gamma >$1000 produce TR photons in the radiator. These photons pass through the drift electrode and enter the gas-filled drift region. Xenon has a typical absorption length of photons in the soft x-ray region of 4 mm to 10 mm [2]. Transition radiation photons thus ionise the gas at the beginning of the drift region. The positive ions drift towards the drift electrode. The electrons drift by the grounded cathode wires towards the anode wires and into the MWPC. Drift electrodes, connected to voltage dividers, on the inner side faces of the drift chamber provide a uniform decrease in voltage throughout the drift region, which facilitates a uniform drift even in regions close to the inner surfaces. The function of the Multi Wire Proportional Chamber is to amplify ionisation. The anode wires are thin ($\Phi = 20 \ \mu m$ [8]); thus electric field strenghts of $10^4 - 10^5$ V/cm are reached.

Electrons create secondary ionisation in the vicinity of the high electric field near the anode wires. A series of such secondary ionisation processes leads to an avalanche of electrons and positive ions near the anode wires. In the secondary ionisations, photons are also produced. These photons cause secondary ionisations. If too many photons cause secondary ionisation, this could result in a self-sustaining current between anode and cathode wires. The MWPC would stop functioning properly. Thus these photons have to be absorbed. Organic gases, which have a good absorption of photons for a wide range of energies, are used to quench these photons. The amplification gain for the ALICE TRD is 3500 [2]. The electrons are absorbed by the positively charged anode wires. The positive ions drift to the grounded pad plane, where they induce a signal. The pad plane of an ALICE TRD consists of 2304 pads, segmented into 16 pad rows and 144 pad columns. The pads have an average size of $7.25 \cdot 87.5 \text{mm}^2$ [2]. The signal on the read-out pads is read out by the front-end electronics.

4.3. Front-End Electronics

The front-end electronics, illustrated in Fig. 4.5, is responsible for the registration of the positive signals induced on the read-out pads. A signal induced on the read-out pads due to a minimum ionising particle passing through the TRD is small: 10^5 to 10^6 positive ions. To minimise signal loss and influences of cable noise, the registration of the signals is carried out as close as possible to the pads themselves. The MCM ("Multi Chip Module"), which contains the front-end electronics, is mounted directly on the back-side of the detector module. The constituents of the front-end electronics are the PASA ("Pre-Amplifier and Shaper") and the TRAP ("Tracklet Processor"). The trap comprises an ADC ("Analogue to Digital Converter"), the TPP ("Tracklet Pre-Processor") and an event buffer.

The signal induced on the pads - the current on a particular pad - is characterised by a sharp rise and a relatively long tail, as shown in Fig. 4.6. This ion tail is due to the relatively small drift velocity of positive ions produced in the avalanches. The PASA first amplifies the signal with a gain of 6.1 $\frac{mV}{fC}$ and then shapes the signal to cancel its tail. The ADC converts the analogue signal coming from the PASA into a digital signal. The signals from the PASA are read out with a sampling rate of 10 MHz; the signal height on each pad is sampled in time bins of 100 ns. Thus, per time bin, the ADC broadcasts a value corresponding to the deposited charge on the pad during this time. The TRAP sets a baseline for the ADC values at an ADC value of 10. The data are stored in an event buffer. In parallel, a cluster finding algorithm in the TPP detects clusters from the acquired ADC data. The TRAP carries out a straight line fit through the clusters: tracklets, a particles track through one TRD chamber, are produced. In addition to that, particle identification is done by analysing the pulse height function (see Chapter 3.4) of the tracklet of the particle. This information is sent to the GTU.
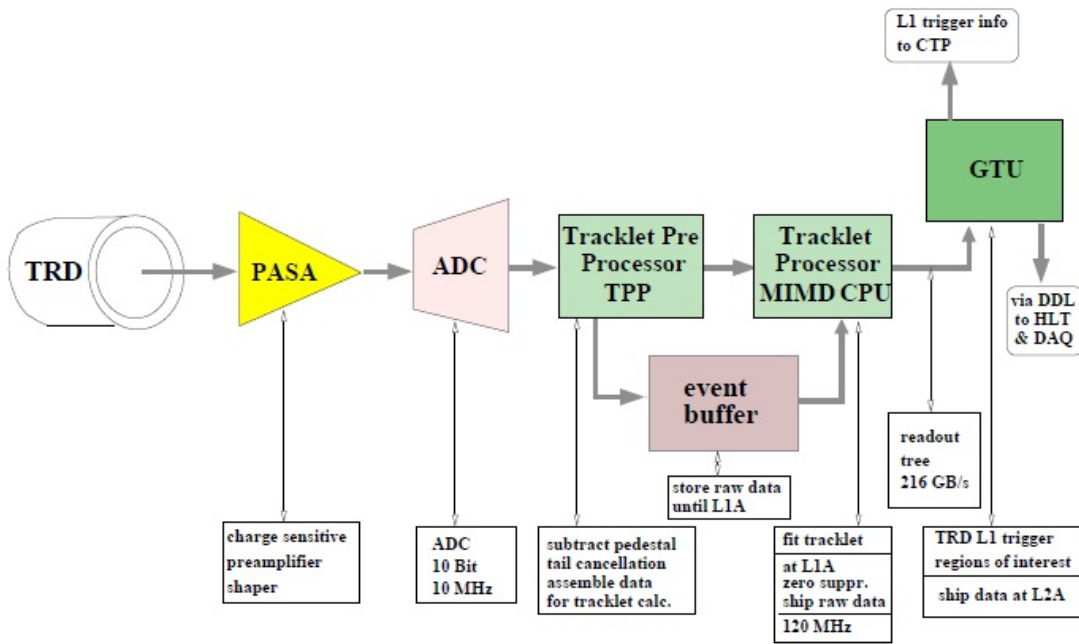
Figure 4.5: Basic logical components of the TRD front-end electronics as used in the TRD at ALICE. The PASA, ADC, TPP, TRAP and the event buffer are contained in one chip, the MCM [2]
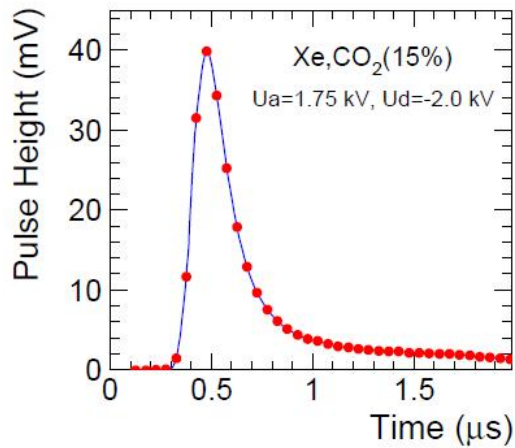
Figure 4.6: Average pulse height on the centre pad. The data were taken during a preliminary run with a prototype TRD chamber using a Fe-55 x-ray source of 5.9 keV [2]
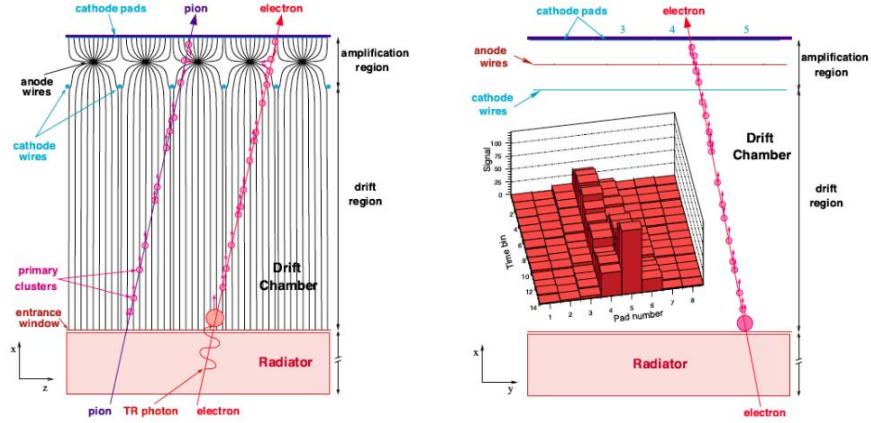
Figure 4.7: Schematic representation of the TRD principle. left.: projection in the x-z plane; schematic view of the signals produced by a pion and an electron. right.: projection in the x-y plane; insert shows for a measured electron track the distribution of pulse height over pads and time bins spanning the drift region (radiation and wire geometry are not to scale) [2]

The left figure in Fig. 4.7 shows a schematic representation of two particles, a pion and an electron, passing through a TRD chamber. The electron, in contrast to the pion, produces transition radiation while traversing the radiator. The right figure in Fig. 4.7 shows the ADC data, i.e. the signal on the pads as a function of pad number and time bin, i.e. drift time, for an electron passing though the TRD. High drift times belong to clusters produced at the beginning of the drift region. Thus the peak due to transition radiation is at a later time bin.

Plotting the pulse height of clusters, i.e. the ADC values summed over adjacent pads, as a function of drift time for a track of a particle, yields a pulse height function. Fig. 4.8 shows average pulse height functions for pions and electrons at the momentum of 1 GeV/c . For electrons, there is a significant increase at later drift times due to transition radiation. On average, the pulse heights of electron tracklets are higher than the pulse heights of pion tracklets. Such pulse height functions are the basis for particle identification.
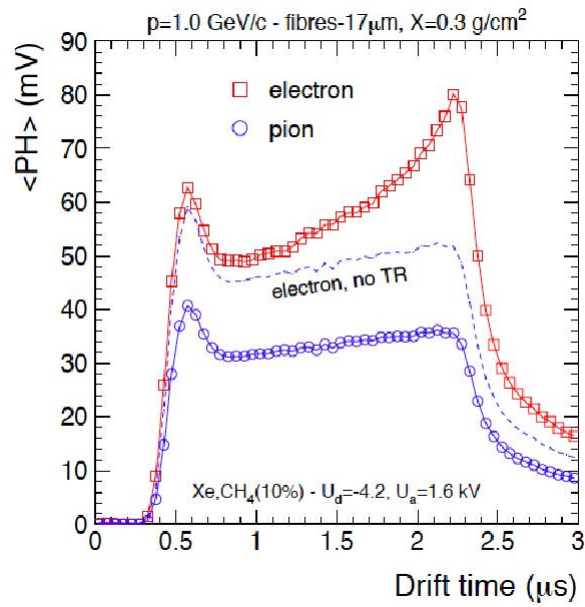
Figure 4.8: Avarage pulse height as function of the drift time for pions and electrons at a momentum of 1 GeV/c for a radiator of 17 μm fibres [2]

5. Cosmic Radiation

The TRD at ALICE detects ionising particles. The TRD prototype chamber, which is commissioned in this thesis project, detects electrons and muons with momenta above 1 GeV/c. Such particles occur naturally on Earth as cosmic radiation [12]. Primary cosmic radiation mainly consists protons [9] irradiating the Earth from galactic sources, e.g. stars. As shown in Fig 5.1, primary cosmic radiation interacts with atoms in the Earth's atmosphere, e.g. Nitrogen or Oxygen, producing further particles, known as secondary cosmic radiation. On the Earth's surface, only products of primary cosmic radiation, mainly muons and in a smaller number, electrons, can be detected.
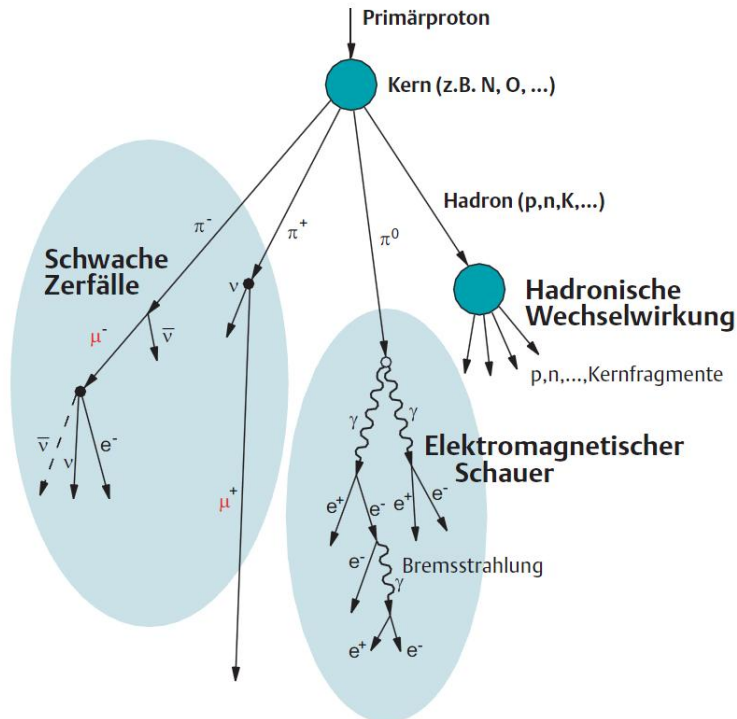
Figure 5.1: Interaction of cosmic radiation in the Earth's atmosphere [14]

5.1. Primary Cosmic Radiation

Primary cosmic radiation incident on the Earth's atmosphere consists of particles produced and accelerated in cosmic sources. Particles incident atmosphere are mainly free protons (79 %) or protons contained in helium nuclei (19 %) [9]; the rest is composed of carbon, oxygen, and iron nuclei as well as electrons (1-2 %), photons and neutrinos [13]. The composition of primary cosmic radiation is well understood. Concerning the sources of primary cosmic radiation, there are many theories [15] [13] The standard argument
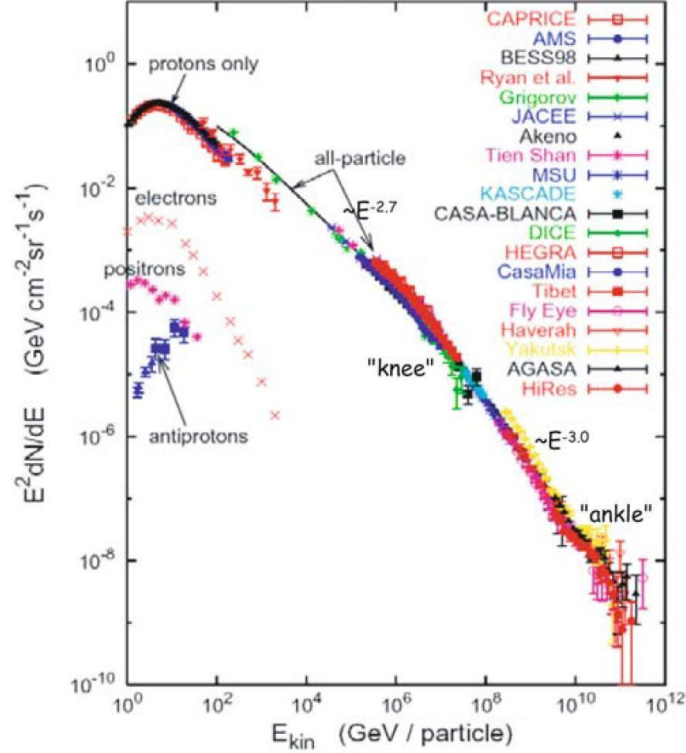
Figure 5.2: Intensity spectrum of primary cosmic radiation [13]

is that low mass stars and supernova explosions are the major sources. The sources of cosmic particles with energies above 10^{11} GeV is not known.

The spectrum of primary cosmic radiation, shown in Fig. 5.2, extends over ten orders of magnitude. The smooth spectrum follows a powerlaw for energies above 10 GeV [13]: $I(E) = \alpha E^{-\alpha}$. The points in the spectrum at which the powerlaw index abruptly changes are called the knee (at 10^6 GeV) and the ankle (at 10^{10} GeV) [15] [13]. Up to the energy at the knee, the powerlaw index is $\alpha \simeq 2.7$; from knee to ankle, the powerlaw index is $\alpha \simeq 3.1$. Data for higher energies is sparse. Still some primary cosmic particles with energies above 10^{10} GeV have been observed even though a cut-off of the flux of particles at 10^{10} GeV, the Greisen-Zatsepin-Kuzmin-Cut-off, is expected [12] [15]. Most of the primary cosmic radiation incident on Earth originates from our galaxy. The energy spectrum, however, indicates that a small portion - high energy cosmic radiation with an energy above 10^9 GeV - also originates from outside our galaxy [12] [13]. Cosmic particles interact with cosmic magnetic fields, e.g. by black holes. As a consequence, cosmic radiation with energies below 10^5 GeV is completely isotropic [12].
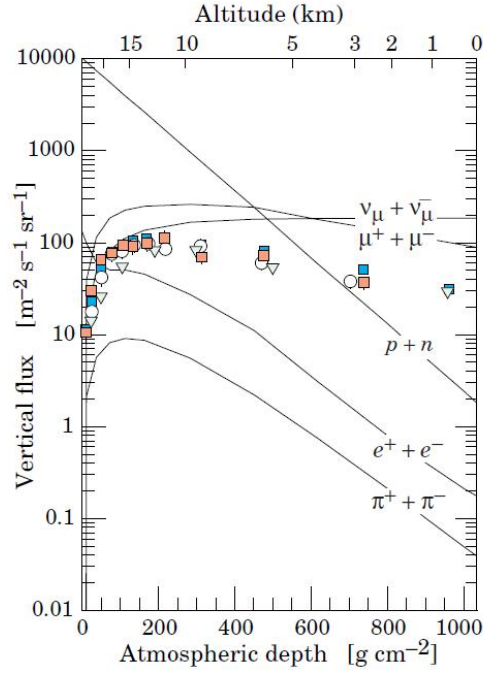
Figure 5.3: Vertical flux of cosmic radiation in the atmosphere with E > 1 GeV. The points show measurements of negative muons with E > 1 GeV [9]

5.2. Secondary Cosmic Radiation

Secondary cosmic radiation is produced when primary cosmic radiation interacts with atoms in the Earth's atmosphere, mainly Nitrogen or Oxygen atoms, as illustrated in Fig. 5.1. The atmospheric depth of the Earth's atmosphere is approximately 1000 gcm^{-2}. Protons have an interaction length of 90.0 gcm^{-2}[12], which means that only approximately 0.02 % of the protons of the primary cosmic radiation reach the surface, as seen in Fig. 5.3. The interaction products are mainly pions and kaons. These are produced in a ratio of 10:1 [12]. Charged pions and charged kaons have an average lifetime of below 1 μs [9]. They decay before they reach the surface. Kaons decay weakly, producing mainly muons, neutrinos and pions, as shown in Tab. 5.1. Neutral pions decay electro-magnetically with a lifetime of below 1 ps [9]. The resultant electromagnetic cascade, the (e,γ)-component , interacts heavily with the atmosphere. Most of the produced electrons do not reach the ground. Charged pions decay weakly, mainly producing muons and neutrinos, as shown in Tab. 5.1. Muons produced in the Earth's atmosphere have a lifetime of $\tau_\pi = 2.2$ μs [9] and may thus decay before they reach the surface Their decay products are electrons and neutrinos. The most numerous cosmic particles inciding on the Earth's surface are muons and neutrinos, as illustrated in Fig. 5.3. The TRD chamber only detects ionising particles; hence only muons are discussed here.

Muons make up approximately 80 % of the charged cosmic particles reaching the

23

PARTICLE	DECAY MODE i	FRACTION N_i/N_0
K^+	$\mu^+ + \nu_\mu$	0.64
K^+	$\pi^+ + \pi^0$	0.21
K^+	$\pi^+ + \pi^+ + \pi^-$	0.06
π^+	$\mu^+ + \nu_\mu$	0.99
π^0	$\gamma + \gamma$	0.99
μ^+	$e^+ + \overline{\nu}_\mu + \nu_e$	1.00

Table 5.1: Decay modes of major contributors to cosmic radiation in the atmosphere (similar for anti particles) [9]

ground, with a mean energy of 4 GeV [9]. Muons incident on the Earth's surface at an angle of $\vartheta \neq 0°$ travel a longer distance in the Earth's atmosphere and are therefore more likely to decay than muons incident at an angle of $\vartheta = 0°$. The flux of muons with an energy of 3 GeV incident on the surface shows an angular distribution of:

$$I = I_{\vartheta=0} \cdot cos^2(\vartheta) \tag{5.1}$$

For muons at higher energies the angular distribution is flatter [9]. The flux of muons at sea level is approximately 1 cm^{-2}min^{-1} [12]. Other particles reaching the Earth's surface in far smaller numbers are protons, electrons, positrons and photons [9].

5.2.1. Extensive Air Showers

Extensive air showers (EAS) are extensive showers of cosmic particles in the Earth's atmosphere [12]. An EAS is caused by a single cosmic particle, whose energy is large enough for its cascade to be detectable on the Earth's surface [9]. This single high energetic cosmic particle interacts with molecules in the Earth's atmosphere in such a way that many energetic hadrons, pions and kaons with a ratio of 9:1, are produced. Neutral pions, the hadronic core of EAS, decay electromagnetically to two photons $\pi^0 \rightarrow \gamma + \gamma$. For high enough pion energies the (e, γ) - component carries enough energy to initiate an electromagnetic shower [9]. Such showers spread over a large area of ground, forming an EAS.

6. Trigger Set-Up

A trigger is a system which decides which events in a particle detector are recorded. Due to limitations on data storage it is not possible to record data continuously and select physically interesting events afterwards. A trigger uses simple criteria to make the decision between physically relevant events and irrelevant events, e.g. due to noise. The function of the trigger in this set-up is to provide a signal each time a cosmic particle passes through the active area of the TRD. The trigger set-up consists of four levels of scintillators and electronic components to analyse the signals coming from the scintillators. The simple criterion is that a cosmic particle has to pass all levels of scintillator nearly simultaneously.

The trigger set-up, shown in Fig. 6.1, consists of two levels of scintillator pads connected to photomultipliers. The TRD is mounted in between the two levels. The electronic components are discriminators, delay units, scalers, coincidence units, and cables connecting these elements. Each of the two scintillator levels consists of two scintillators, which are mounted at right angles to each other, as illustrated in Fig. 7.6. The overlapping area of the scintillators thus fits the active area of the TRD chamber. To reduce the effect of noise, the discriminators analyse the signals coming from the photomultiplier tubes. To select physically relevant events, the scintillators are operated in coincidence.
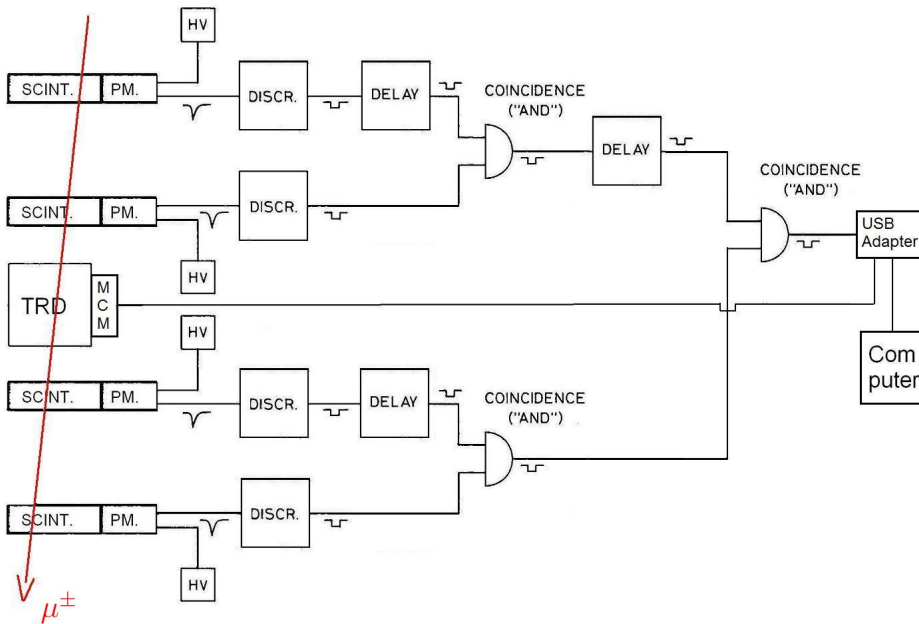
Figure 6.1: Schematic representation of trigger set-up

Fig. 6.2 shows the actual electronic trigger set-up. The scintillators are connected to discriminators. The discriminators select incoming analogue signals with a minimum signal height and convert these analogue signals into logical signals. The logical signals are delayed before they reach coincidence units. The coincidence units check whether two signals are coincident in time, and if they are, a logical signal is triggered. These logical pulses are counted with a scaler. Before the logical signals are used as trigger signals, they are converted from the NIM to the TTL standard by a NIM to TTL converter. The next chapters describe the scintillator assemblies (Chapter 6.1), their commissioning (Chapter 6.2), the individual electronic units used in the set-up (Chapter 6.3) and their adjustment (Chapter 6.4, Chapter 6.5, Chapter 6.6).
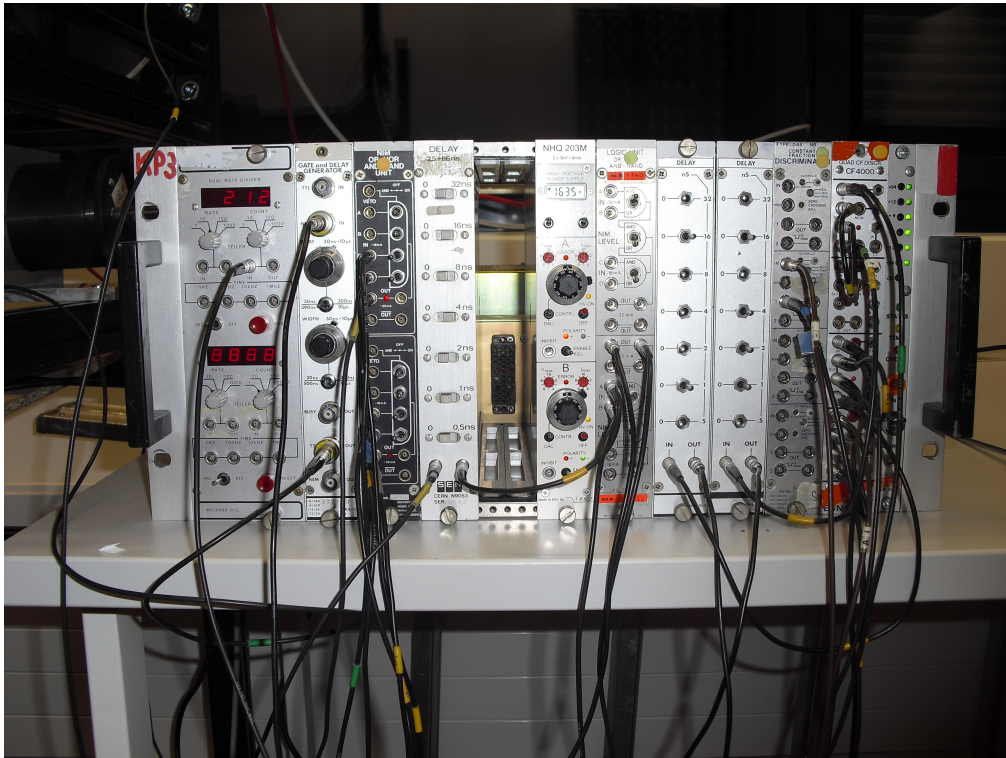
Figure 6.2: Picture of electronic trigger set-up. From left to right: scaler, NIM to TTL converter, coincidence unit, delay unit, empty slot with rear power connector, high voltage power supply, coincidence unit, delay unit, delay unit, discriminator, discriminator

6.1. Scintillator Assemblies

Scintillators are particle detectors which produce a flash of light when an ionising particle passes through them. Scintillator set-ups usually consist of a scintillator, a light guide

and a photomultiplier tube. Their principle of operation is the following. An ionising particle passes through the scintillator. In the scintillator material a small flash of light is produced, which is transmitted through the scintillator via a light guide to a photomultiplier tube. The photomultiplier tube, on the one hand, converts single photons into an analogue electrical signal and, on the other hand, it amplifies this signal. For a minimally ionising particle, such a set-up produces a signal of a few hundred mV at the output of the photomultiplier.

Scintillators have two primary functions: converting the energy deposited by an ionising particle into a light flash and transmitting this light to a photomultiplier tube. To achieve these two goals a wide variety of materials can be used, categorised here according to similar principles of operation: organic materials, inorganic crystals, gases and glasses [11]. In our experimental set-up organic plastics are used and therefore discussed here. This scintillator type consits of solutions of organic fluorescent material in a solid plastic solvent. The primary fluorescent material, usually PBD[1] , p-Terphenyl [2] or PPO [3] [11], is responsible for converting the deposited energy into a flash of light. An often used secondary solute, POPOP[4], functions as a wavelength shifter, which inhibits the re-absorption of photons by the organic materials [8].

Scintillation light in organic scintillators is emitted when an ionising particle passes through them. The particle interacts with the molecules of the scintillator compound; the valence electrons of the molecules are excited to an energetically higher state. Falling back to an energetically lower state, photons with energies in the UV region, characteristic for a molecule spectrum, are emitted [16]. The light output of the molecules follows the simple exponential decay of fluorescent radiation with decay times of a few ns, as illustrated in Fig. 6.5 [11]. Photons with energies in the UV region, i.e. a few eV, and hence wavelengths of around 300 - 400 nm have absorption lengths of a few mm in most organic materials [8]. Wavelength shifters used in plastic scintillators absorb UV radiation and emit visible light. According to the Bethe-Bloch formula, a minimum ionising muon deposits approximately 1.7 - 2 MeV per cm scintillator material [9]. Only a few percent of the deposited energy is converted into photons. Thus in plastic scintillators a particle has to deposit approximately 100 eV per emitted photon. Per minimum ionising muon, approximately $2 \cdot 10^4$ photons are emitted.

Scintillator light has to be transmitted from the molecule responsible for its emission to the photo cathode in the photomultiplier. Within the scintillator the transport proceeds through total reflection on the scintillator faces. In Chapter 6.2, we discuss how to facilitate total reflection on the scintillator faces. Usually none of the scintillator faces matches the area covered by the photo cathode. There are two possibilities in attaching the scintillator to a photomultiplier tube. The first one is to directly attach the photo-

---

[1] 2-phenyl,5-(4-biphenylyl)-1,3,4-oxadiazole ($C_{20}H_{14}N_2O$)

[2] $C_{18}H_{14}$

[3] 2,5-diphenyloxazole ($C_{15}H_{11}NO$)

[4] 1,4-Bis-[2-(5-phenyloxazolyl)]-benzene ($C_{24}H_{16}N_2O_2$)
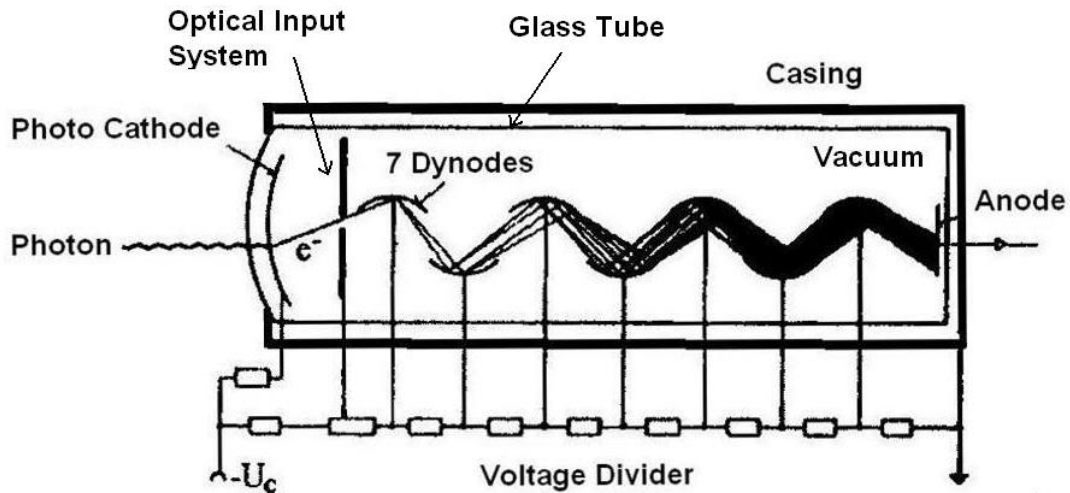
Figure 6.3: Schematic representation of a photomultiplier tube [8].

multiplier to the smallest face of the scintillator As a result, the photo cathode usually covers only a fraction of the scintillator's face and consequently only a fraction of the scintillator light reaches the photo cathode. The second possible way is to use a light guide, usually made of plexiglas, to transport the scintillator light to the photomultiplier. Light enters them from one end, and via internal reflection it is guided to the other end [11]. They can be customised to perfectly fit the scintillator and the photo cathode.

6.1.1. Photomultiplier Tube

The purpose of a photomultiplier tube is to transform a typically weak light signal into a measurable electrical signal. A standard photomultiplier tube transforms such a light signal into an electrical signal of a few hundred mV, which is strong enough to be measured despite electrical noise.

Photomultiplier tubes consist of the following elements , as shown in Fig. 6.3 : a photo cathode, an electron optical input system, a number of dynodes, a voltage divider, an anode, a glass tube and a casing [11]. Photons incident on the photo cathode produce electrons via the photoelectric effect. Hereby the energy of the photons has to be above the work function of the cathode material. To select the proper cathode material, it is helpful to have a look at the efficiency of the photo cathode. Usually these numbers are supplied by the manufacturer. The quantum efficiency is defined as the number of photoelectrons released divided by the number of incident photons on the cathode as a function of the wavelength of the incident photon [11]. An example would be the quantum efficiency of a Hamamatsu R580, shown in Fig. 6.4. This photomultiplier,

28
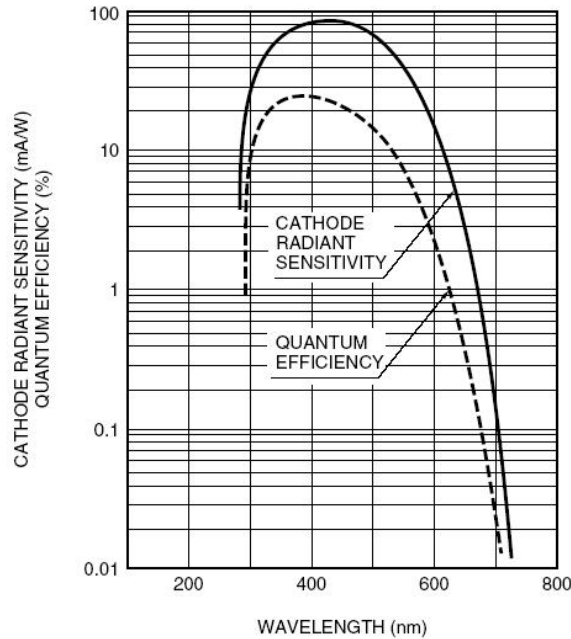
Figure 6.4: Quantum efficiency of a Hamamatsu R580 photomultiplier tube [www.hamamatsu.com]

for example, can be used efficiently for scintillators emitting photons with wavelengths between 300 nm and 650 nm with a peak efficiency of 25 % at approximately 400 nm.

The electron optical input system consists of focusing electrodes, which focus the emitted photoelectrons on the first dynode. The dynode system amplifies the weak photo-electric current. There is usually a potential difference of a few kV between the first dynode and the anode. Voltage dividers are used to realise equal potential differences of 100 - 200 V between the separate dynodes. The dynode system relies on the principle of secondary emission. The electrons emitted by the photo cathode are accelerated towards the first dynode. Energy is transferred to the electrons within the dynode material and a number of secondary electrons is emitted. This process is repeated for each dynode, resulting in multiplication factors of up to 10^8, which means that for each electron leaving the photo electrode, 10^8 secondary electrons produce an electrical signal at the anode. Depending on the applied high voltage and the output impedance, the signal which a minimum ionising muon produces at the output of the photomultiplier has a strength of a few hundred mV. The glass tube holds the vacuum. The casing shields the photomultiplier tube from environmental influences, e.g. magnetic fields or ambient light. Fig. 6.5 shows a comparison of a light output of a scintillator and an electric output of a photomultiplier tube for different rise times. The signals show some common features: both exhibit a rapid rise time and an exponential decay. For the scintillator this is the exponential decay of fluorescent radiation with decay times of a few ns. The photomultiplier responds to single photons. As a consequence, the signal

29
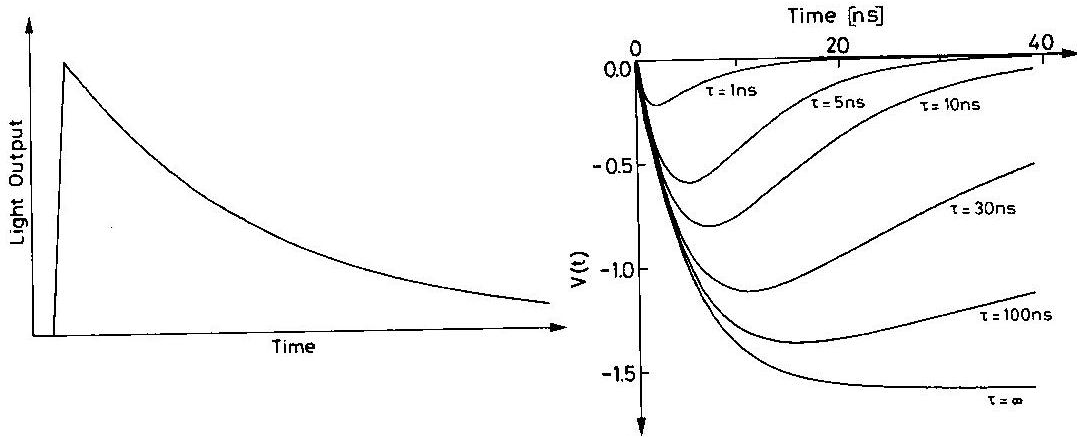
Figure 6.5: left: scintillator light output [11]. right: photomultiplier electric output for different rise times. Negative high voltage is applied to the photomultiplier [11]

at the photomultiplier's output resembles the signal of the scintillator.

6.2. Scintillator Commissioning

In a scintillator assembly, visible light is transported through the scintillator to the photocathode of the photomultiplier tube. This makes such a scintillator set-up highly susceptible to ambient light. To shield the set-up from ambient light, it is wrapped in black tape. Another source of signal distortion comes from external magnetic fields. The secondary electrons which are accelerated between the dynodes can be deviated from their nominal trajectories by magnetic fields and might not reach the next cathode. To shield photomultiplier tubes from external magnetic fields, casings are used. An often used material for casings is mumetal©, which consists of a nickel iron alloy.

Light is transported in the scintillator pads via reflection on the scintillator faces. To make this transport more efficient, the probability for total reflection on the scintillator faces is maximised. If light impinges on a surface between an optically thicker medium and optically thinner medium at an angle θ, total reflection occurs at an angle larger than the Brewster Angle θ_c [16].

$$\sin \theta_c = \frac{n_{out}}{n_{scint}} \tag{6.1}$$

n_{scint} and n_{out} are the refraction indices for the optically thicker and thinner media, respectively. To keep θ_c as small as possible, an optically thin medium has to surround the scintiallator material. Air has a relatively low refraction index of $n \simeq 1$. Thus

30
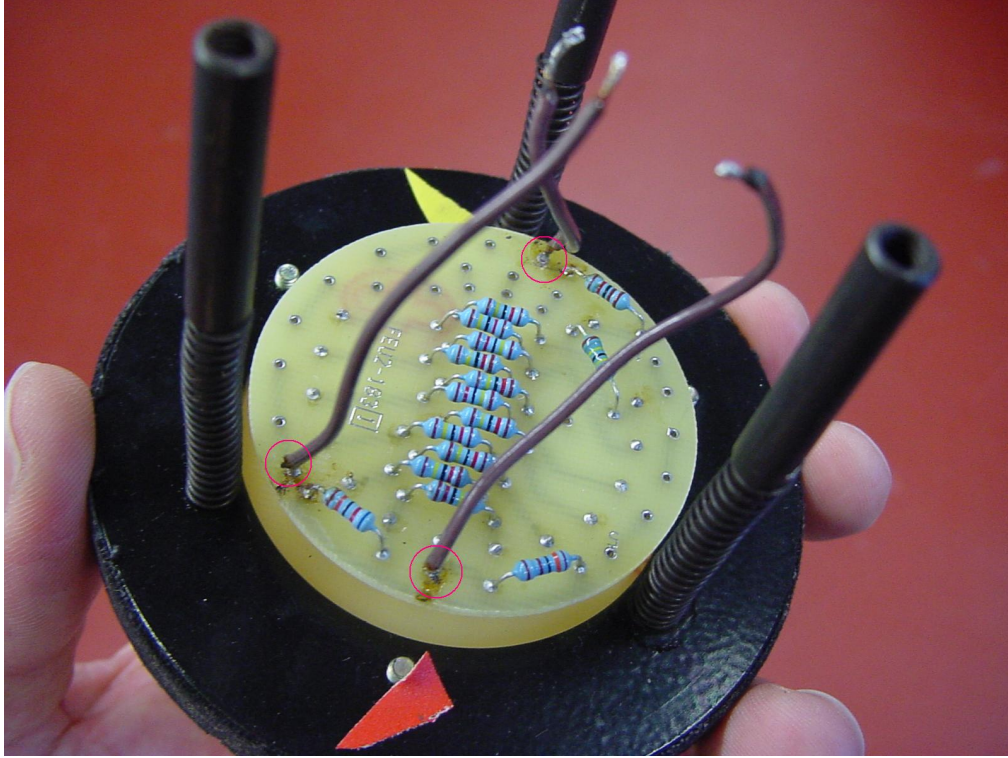
Figure 6.6: The photomultiplier base with voltage dividers and soldering joints. The soldering joints which were fixed are marked by a red circle

to facilitate total reflection on the scintillator faces, the scintillator material is loosely wrapped in black tape so that there is a layer of air between the scintillator material and the tape. Light impinging on the scintillator faces at an angle smaller that θ_c is partially reflected and the remainder is transmitted. To redirect this transmitted light back towards the scintillator, a layer of material, with good reflection characteristics, is inserted between the scintillator material and the black tape. Teflon, aluminium foil or white paper have such good reflection characteristics.

The scintillators used in this set-up were delivered fully assembled, as they had been used in previous experiments. Still, they had to be checked whether they were functioning properly. Before applying high voltage to the photomultiplier, the base and voltage divider were examined, as shown in Fig. 6.6. For two of the scintillators in this set-up, soldering joints were damaged and had to be fixed.

If there is no further apparent damage to the base and the voltage divider, high voltage can be safely applied to the photomultiplier. While raising the voltage, the current has to be monitored. Big leaps in the current are an indicator of a malfunctioning electronic circuitry in the photomultiplier. The next thing to check is whether the scintillator is susceptible to ambient light. To do this, the scintiallator assembly is connected to an electronic circuitry which counts the number of analogue pulses at the output of the

Figure 6.7: The whole scintillator assembly as it is used in the experiment. From left to right: scintillator pad beneath black tape; light guide beneath black tape; photomultiplier beneath mumetal© shielding; high voltage connector and signal output connector. The whole scintillator assembly is 870 mm long

scintillator assembly. Such an electronic set-up consists of a discriminator and a scaler (both are described later on in chapter 6.3). The count rate is examined while switching the room light on and off and closing the blinds. If there are significant changes in the count rate, the outer protection of the scintillator assembly has to be renewed. This was the case for two of the scintillators used in this set-up. To remedy the protection, it was taken off and a new layer of black tape was applied. Especially the edges of the scintillators require special care, as their protection is easily damaged during transport. Fig. 6.7 shows a complete scintillator assembly as it is used in the experiment.

6.3. Electronics Set-Up

The electronic set-up consists of modules which process electrical signals. The units used in this set-up all conform to the NIM (*Nuclear Instrument Module*) standard. All units are produced in the form of modules which fit into power bins, or power crates. The bin, as well as the module dimensions are standardised. Modules are inserted into slots and powered by rear power connectors. The NIM standard requires the rear power connectors to provide the following voltages: $\pm$ 6 V, $\pm$ 12 V and $\pm$ 24 V. The modules used in this set-up are discriminators, delay units, coincidence units, and scalers and a NIM to TTL converter, as shown in Fig. 6.2.

6.3.1. Discriminators

The main function of discriminators is selecting incoming analogue signals with a minimum signal strength and converting these analogue signals into logical signals, rectangular pulses. Only incoming signals whose amplitude exceeds the threshold trigger a signal from the discriminator [11]. The threshold voltage is usually adjusted via a potentiometer on the discriminator's front face. For the discriminators in this set-up, the threshold could be adjusted in a range from 0 mV to 200 mV. A discriminator filters out low amplitude noise coming from devices such as photomultiplier tubes. A preferred practice in the NIM convention for high count rates and fast timing - as is the case here in this experiment - is to use the voltage levels 0 V and -0.8 V for logic 0 and logic 1, respectively [11]. The width of this signal can usually be adjusted as well on the discriminator's front side.

Timing plays a crucial role in the whole trigger set-up. Timing refers to the measurement of very small time intervals [11], or, more specifically in this set-up, the resolution in time with which two coincident signals can be measured. Two effects limit the time resolution of discriminators: *walk* and *jitter*, as illustrated in Fig. 6.8 .
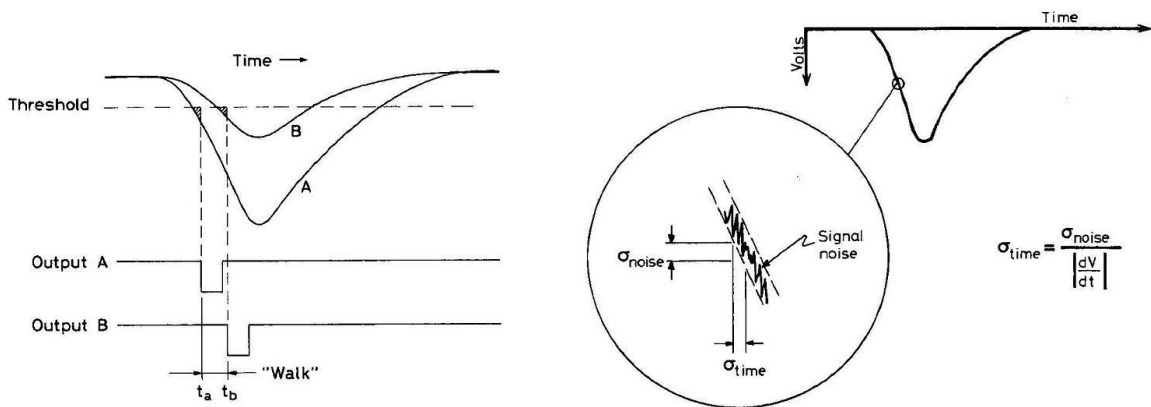
Figure 6.8: left.: Illustration of walk effect with two coincident signal of different height; right.: Illustration of jitter effect (noise) [11]

The effect of walk is depicted in the left figure in Fig. 6.8; two coincident signals trigger a discriminator's response at different times. In leading-edge triggering, discriminators broadcast a signal if a certain threshold value is exceeded. Coincident pulses with different heights thus trigger a discriminator response at different times; formerly coincident signals pass through the electronic set-up with a time difference $\Delta t = t_b - t_a$. A remedy for walk effects is *Constant Fraction Triggering*, which means that the trigger level is set at a constant fraction or percentage of the signal height, usually at 50 % [11]. A constant fraction discriminator triggers at 50 % of the height of incoming pulses, and thereby effects of walk are minimised. Jitter, as shown in the right figure in Fig. 6.8,
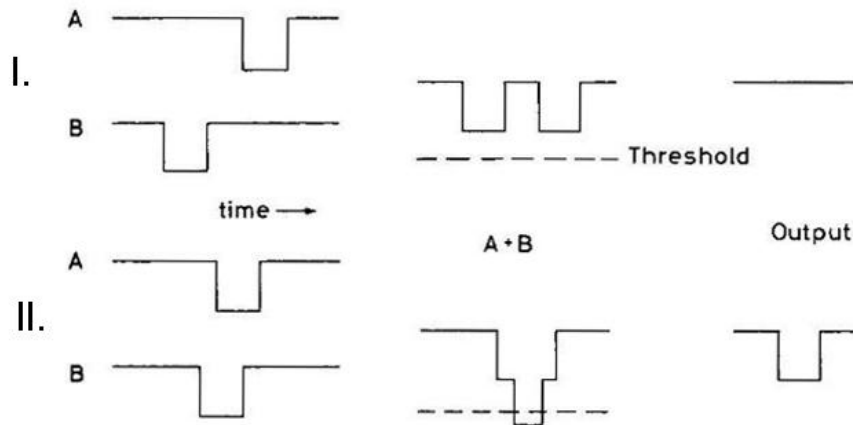
Figure 6.9: Illustration of summing method of determining coincidence between two signals. Signal A and B are added. In case I. the signals do not overlap in time and do not pass the discriminator threshold. In case II. the signals overlap in time and pass the discriminator threshold [11]

refers to the effect noise has on timing. Especially for photomultipliers, effects of noise are small compared to effects of walk. Still noise can never be completely eliminated; jitter constitutes a limitation for time critical measurements.

6.3.2. Delay Units

Delay units delay signals by an adjustable time. Delay units consist of variable lengths of cable [11]. To propagate through a given length of cable, signals need a certain amount of time. Switches on the delay box's front face set through how much cable signals propagate in the box. NIM delay units, usually allow a delay between 0 ns and 64 ns. An analogue electric signal propagates through cables with a speed of 1 m/ns. Especially in coincidence measurements, the use of delay units is mandatory.

6.3.3. Coincidence Units

Coincidence units determine whether two logical signals are coincident in time. If they are, they send out a logic 1. If they are not, they send out a logic 0 [11]. There are a few techniques to determine coincidence. The most commonly used is to add incoming signals and send the added signal through an internal discriminator unit with a threshold just beneath the sum of the signals. If the signals overlap in time within a specified time interval (for the units used in the set-up the coincidence time is 4 ns), they trigger a discriminator response, as illustrated in Fig. 6.9 .
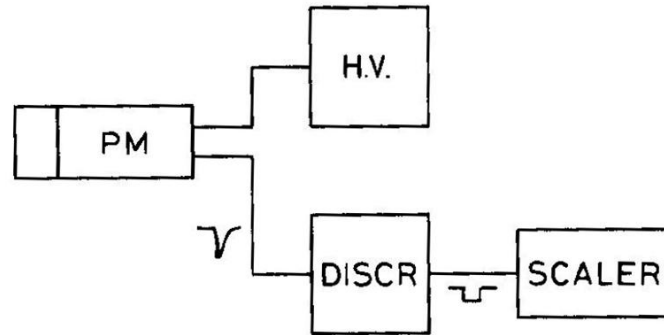
Figure 6.10: Set-up for a plateau measurement: scintillator assembly connected to a high voltage power supply, discriminator, scaler. [11]

6.3.4. Scalers

Scalers are units which count incoming logical signals. Incoming logical signals increment a counter on the scaler's display. They constitute a convenient way of counting the number of logical signals coming from an electronic set-up.

6.3.5. NIM to TTL Converters

NIM to TTL (*Transistor Transistor Logic*) converters convert incoming logical signals from the NIM to the TTL standard. In the NIM standard, a voltage level of -0.8 V is used for logic 1. In the TTL standard, a voltage level of 2 V is used for logic 1. The trigger input of the TRD read-out system responds to TTL signals. The trigger signal from the NIM crate has to be converted from the NIM to the TTL standard.

6.4. Adjusting the PM Voltage: A Plateau Measurement

Photomultipliers are operated with high voltage; a wide range of possible voltages can be applied to their dynode system. Usually the manufacturer of the tube recommends a working voltage for a particular tube, which can be used as a starting point for a finer adjustment of the applied voltage. A simple procedure to find the exact working voltage suited for a specific application - and radiation - is a plateau measurement [11]. Fig. 6.10 shows the set-up for such a measurement. A wide range of voltages is applied to the photomultiplier tube. A discriminator analyses the signal coming from the tube. Each time the discriminator sends out a signal, the scaler counter is incremented.

Such a plateau measurement yields a result as, for example, in Fig. 6.11 for one of
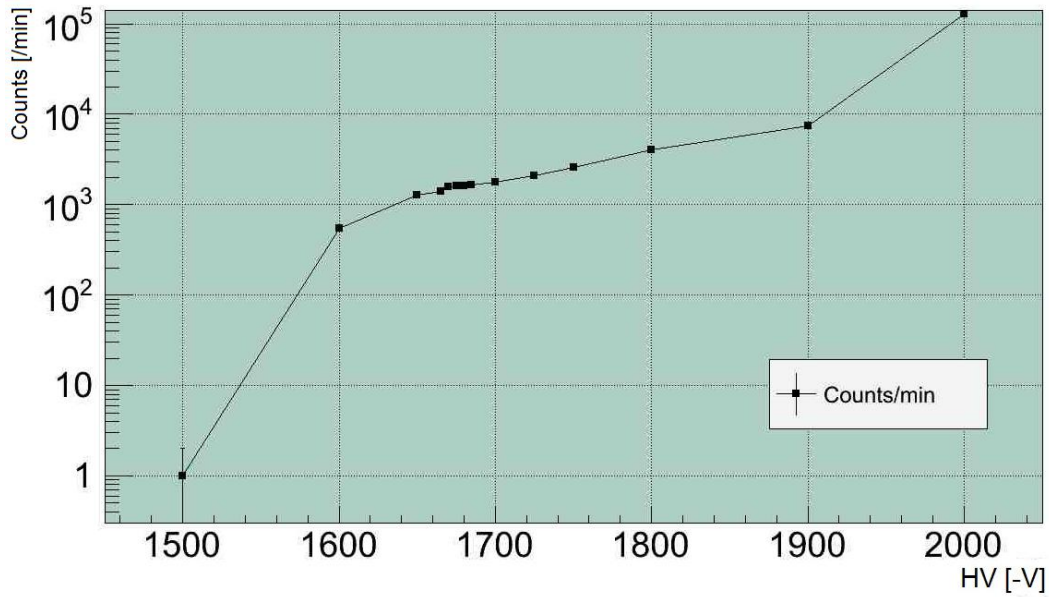
Figure 6.11: plateau measurement for scintillator PMT-03

the scintillators used in the setup, PMT-03. The discriminator connected to PMT-03 is used with a threshold of $U_{th} \simeq$ -10 mV so that nearly all signals coming from the tube pass its threshold. The processes leading to signals from the scintillator assembly are atomic processes with a very small probability of success and very high number of trials. The Poisson distribution describes such processes. The error on the number of counts n is $\sqrt{n}$ [11]. Below voltages of $\simeq$ -1500 V, the signals coming from the photomultiplier tube are not strong enough to pass the discriminator. Below -1600 V, there is a sharp rise in the count rate. More and more signals from the tube pass the discriminator. At -1600 V a plateau in the count rate is reached. All particles of the incoming radiation trigger a signal strong enough to pass the discriminator and thus the count rate depends only little on the applied voltage. At -1800 V, there is again a sharp rise in the count rate. Noise is amplified beyond the discriminator threshold. In addition to that, there are regeneration effects in the tube [11]. There is a small region in the plateau, $U_{HV} \simeq$ - (1670 - 1685) V, in which the count rate depends the least on small changes in the applied voltage. It is quite convenient to set the applied voltage within this region, at -1675 V, as this ensures a minimum of counting variation due to changes in the voltage between single dynodes. This procedure has to be repeated for all of the other scintillators in the set-up; a voltage of -1710 V is applied to PMT-01, -1600 V to PMT-02, and -1710 V to PMT-04. The results for the respective plateau measurements are presented in Appendix A.2.
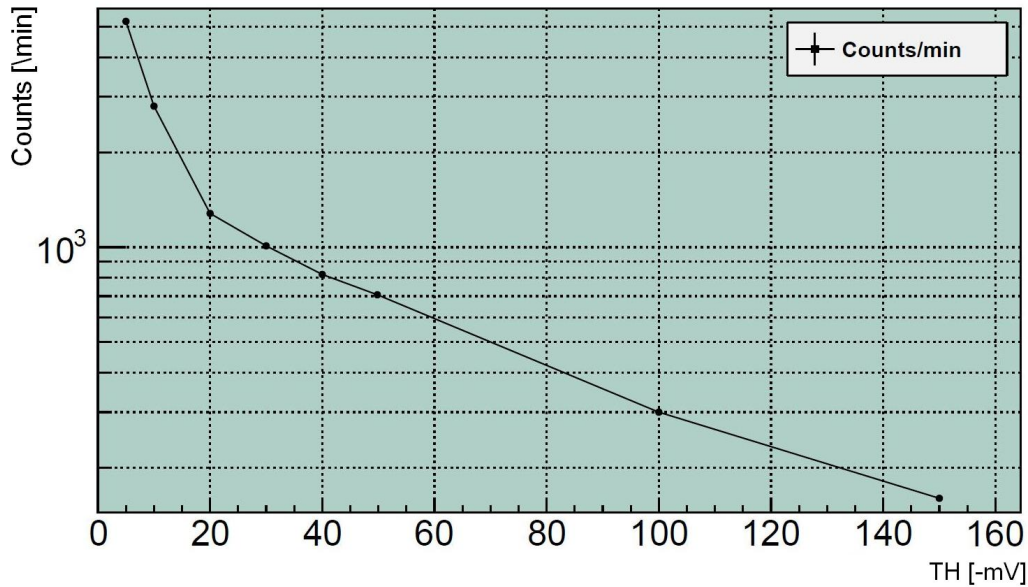
Figure 6.12: Adjusting the discriminator threshold for scintillator PMT-03: measuring the count rate as a function of the discriminator threshold

6.5. Adjusting the Discriminator Threshold

A discriminator only sends out a signal if an incoming signal exceeds its threshold. The discriminators used in the set-up have a threshold which can be adjusted via a potentiometer from 0 mV up to -200 mV. The signals coming from the scintillators were displayed via an oscilloscope; most of them are between -30 mV and -200 mV. Thus, a reasonable threshold may be -20 mV. To validate this guess, the count rate as a function of the threshold voltage is measured. The set-up is the same as for the plateau measurement, as illustrated in Fig. 6.10. For PMT-03, at a working voltage of -1675 V, this result of this measurement is shown in Fig. 6.12.

Below a trigger threshold of -20 mV, the influence of noise and other small signals coming from the photomultiplier tube is high. Above a threshold of -20 mV, physically relevant signals are cut off. For PMT-03, a trigger threshold of -20 mV is chosen. This measurement has to repeated for all scintillators and discriminators used in the experiment. For each discriminator a threshold of -20 mV is used. The results are presented in Appendix A.3.

6.6. Adjusting the Coincidence Units

Coincidence units are used to further reduce the effect of noise on measurements in nuclear and particle physics. Coincidence in time helps to single out physically relevant
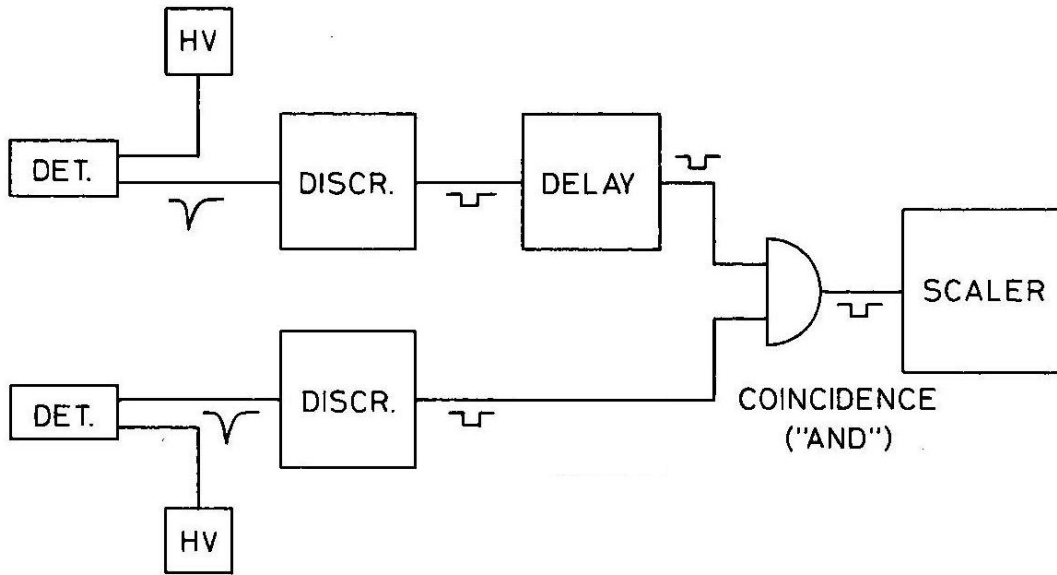
Figure 6.13: Simple coincidence circuit for two scintillators ("DET.") (adapted from [11])

events [11]. In this experiment a physically relevant event is a cosmic particle passing through the two levels of scintillators, which are geometrically arranged in a way so that such a cosmic particle also passes through the TRD's active area. If a particle passes through all of the four scintillators, a trigger signal is produced. The signals of cosmic particles pass through the whole trigger set-up - the scintillator, photomultiplier tube, discriminator and cables - before it reaches a coincidence unit. The connections between the single scintillators and the coincidence units have different lengths and thus the signals from different scintillators originating from one cosmic particle have different transmission times to the coincidence units. Only signals which overlap for approximately 4 ns trigger a signal in the coincidence unit. To compensate for different signal transmission times, delay units are used. In the end, only physically relevant events, corresponding to single cosmic particles passing through the scintillator pads and the TRD, are supposed to trigger a signal which initiates the read-out of the TRD data. Fig. 6.13 depicts a standard coincidence circuit.

To calibrate the coincidence units, secondary cosmic particles can be used. Their velocity is sufficiently close to the velocity of light. Each of the two levels of scintillator pads has to be adjusted on its own before coincidence between the two levels can be adjusted. Exemplary, the calibration of the upper level is described here. A standard coincidence circuit, as shown in Fig. 6.13, is set up with PMT-01 and PMT-02 connected to one of the discriminators, respectively. The scintillator pads are arranged perpendicular to each other with an overlapping area of $9 \cdot 10$ cm^2. The aim is to measure the number of coincident signals, i.e. coincidences, as a function of delay between the signals coming from the different scintillators. The result is the distribution shown in Fig. 6.14.
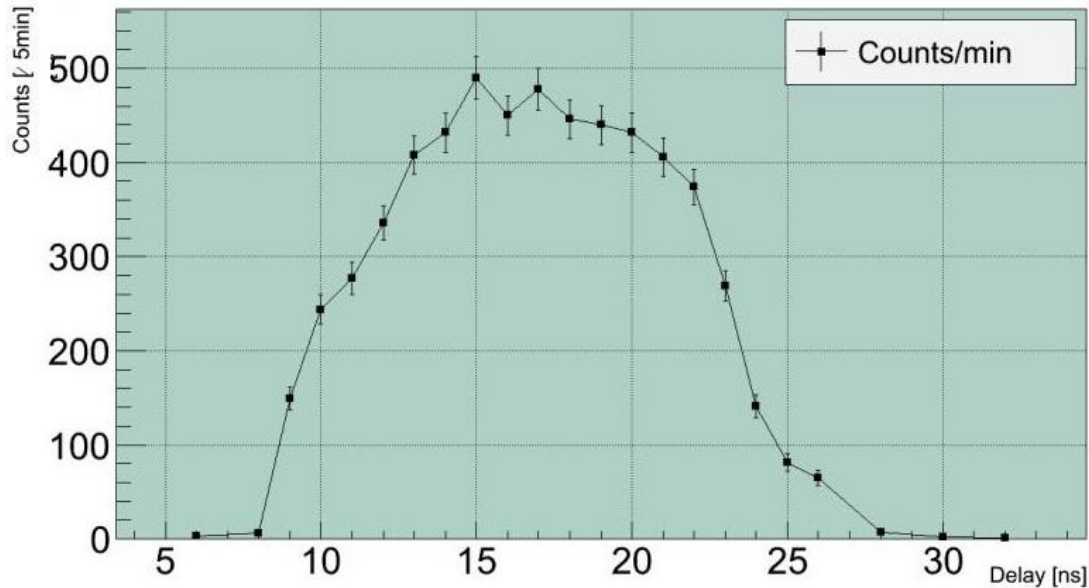
Figure 6.14: The coincidence curve for the upper level: The number of coincidences as a function of the delay between the scintillators in the upper level

The correct setting of the delays is in the middle of the plateau. For the upper level, this means setting the delay at 17 ns. There is a simple check whether the coincidence system is working properly. To have coincidences, the signals coming from the discriminators have to overlap for a small period of time. The signals coming from the discriminators used in this experiment have a signal width of $\simeq$ 12 ns. The range in which there are coincident signals is $\simeq$ 20 ns, which corresponds to the idea that the two signals have to overlap for a minimum period of time - here 4 ns. The same procedure has to be repeated for the lower level. The result is in Appendix A.4. Here, the delay between the scintillators is set at 22 ns. Another check whether the set-up is working can be performed at this stage. The flux of muons at sea level is approximately 1 cm^{-2}min^{-1}. The scintillators in each level have an overlapping area of approximately 90 cm^2. Thus the flux of myons through this area is 90/min. The scintillators in the upper level detect approximately a flux of approximately 90/min. The measured value is close to the theoretical one. This ensures that the set-up is working correctly at this stage.

The last step in configuring the trigger set-up is to calibrate the coincidence set-up between the upper and the lower level of scintillator assemblies. The maximum value of coincidences for both scintillator levels - approximately 13/15 min - is small compared to the maximum value of coincidences for each of the levels. The coincidence set-up for both levels detects only muons from a solid angle range smaller than the range for each of the levels, which is nearly 2π. The delay between the two levels is set at 20 ns. The rate of random coincidences N_r, i.e. coincidences due to uncorrelated signals, follows from the rates from the single branches N_i and the width of the signals σ from these:
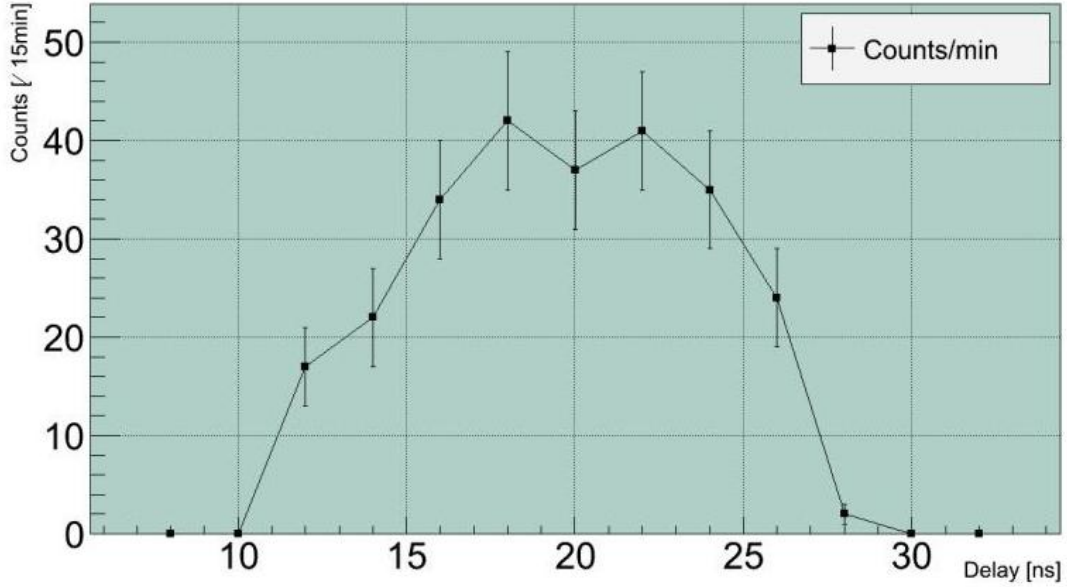
Figure 6.15: The coinicidence curve for both levels: the number of coincidences as a function of the delay between the two levels

$N_r = \sigma \cdot N_1 \cdot N_2$. For this set-up, the rate of random coincidences is approximately $2.5 \cdot 10^8$ Hz. This low rate ensures that random coincidences do not have an effect on the performance of the trigger.

6.7. Performance Measurement: Angular Dependence of the Flux of Cosmic Radiation

A performance measurement was carried out to ascertain that the whole trigger set-up was working properly. The angular dependency of cosmic radiation was measured. The angular distribution of the muon intensity with an energy of 3 GeV at the ground is $I(\vartheta) = I_{\vartheta=0} \cdot cos^2\vartheta$, as explained in Chapter 5.2. The count rate of the coincidence set-up was measured as a function of the angle between the two levels ϑ. Mechanical restraints restricted the angle range of the measurements: the measured angle range is not symmetric. Geometrical effects, which influence the count rate, have been taken into account. While moving the overlapping areas of the levels to fix an angle ϑ between them, the levels were not turned. As a result, the effective overlapping area becomes smaller as a function of ϑ, as illustrated in Fig. 6.16:

$$\cos(\vartheta) = \frac{A_{eff}(\vartheta)}{A_{eff}(\vartheta = 0)} \tag{6.2}$$

The measured count rates have to multiplied by a factor $\frac{1}{\cos(\vartheta)}$ to account for this effect. The measured data points reflect the theoretical distribution well, as shown in Fig. 6.17 . At this point we can be reasonably sure that the trigger set-up performs adequately. With a high efficiency, cosmic radiation, mainly muons, passing through both levels of scintillator, and thus the active area of the TRD, trigger a signal which is used for a read out of TRD data.
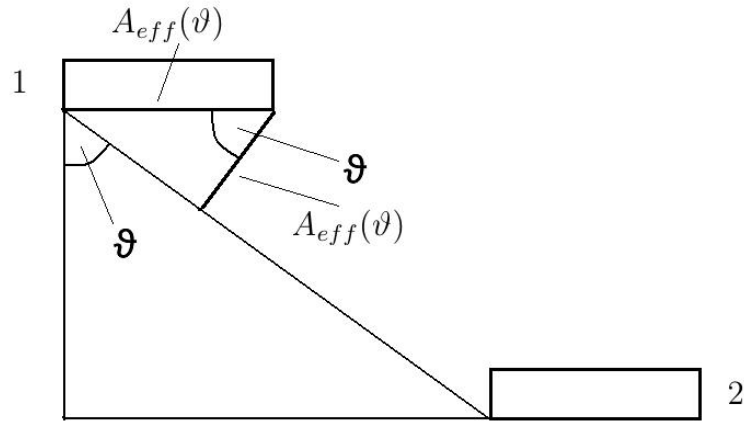
Figure 6.16: Schematic representation of the measurement of the angular dependence of the flux of cosmic radiation. ϑ is the angle between the overlapping area of scintillator level 1 and level 2
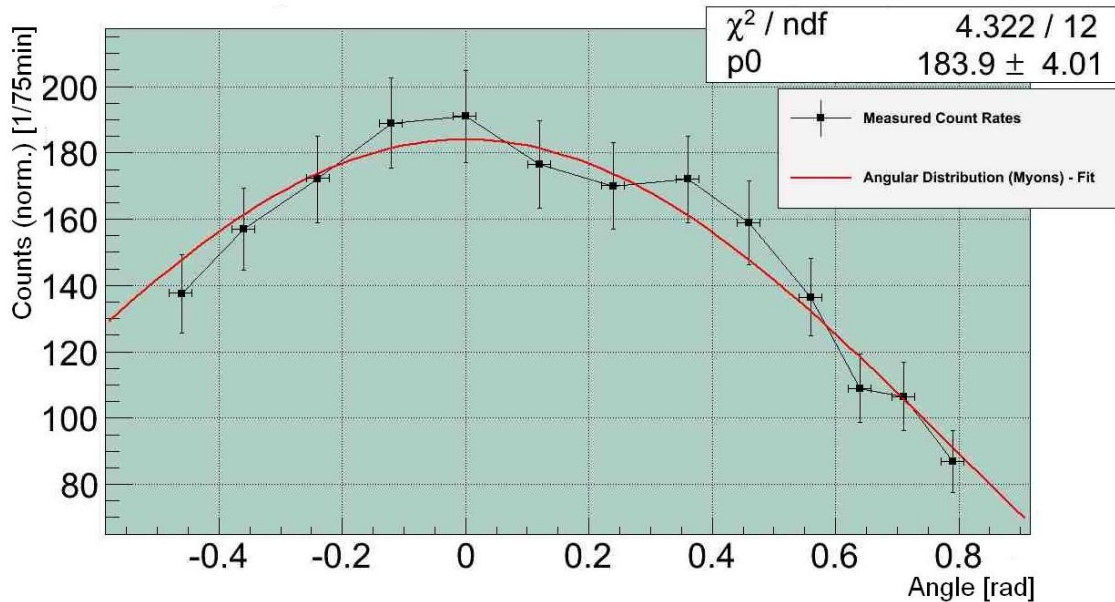
Figure 6.17: Measurement of the angular distribution of the flux of cosmic radiation. The error on the angle has been estimated from the scintillator pad geometry

7. Commissioning of the TRD Prototype Chamber

The first part of the commissioning of the TRD chamber is presented in this chapter: supplying the chamber with the appropriate gas and the electrics with high voltage, as well as checking whether the chamber's electric circuitry is operational. Then the individual components are fit into the mechanical installation. Fig. 7.1 shows two pictures of the chamber used in the project. On the left side, there is a picture of the chamber's front side with the entry window for particles. On the right side, there is a picture of the chamber's back side with the connectors to the read-out pads. The read-out pads are beneath a layer of carbon fibre reinforces Rohacell ©. The chamber has two gas connectors, one for the gas inlet and one for the waste gas outlet. There are also two high voltage connectors, one for the drift electrode and the other for the anode wires. The connector to the cathode wires has to be grounded.
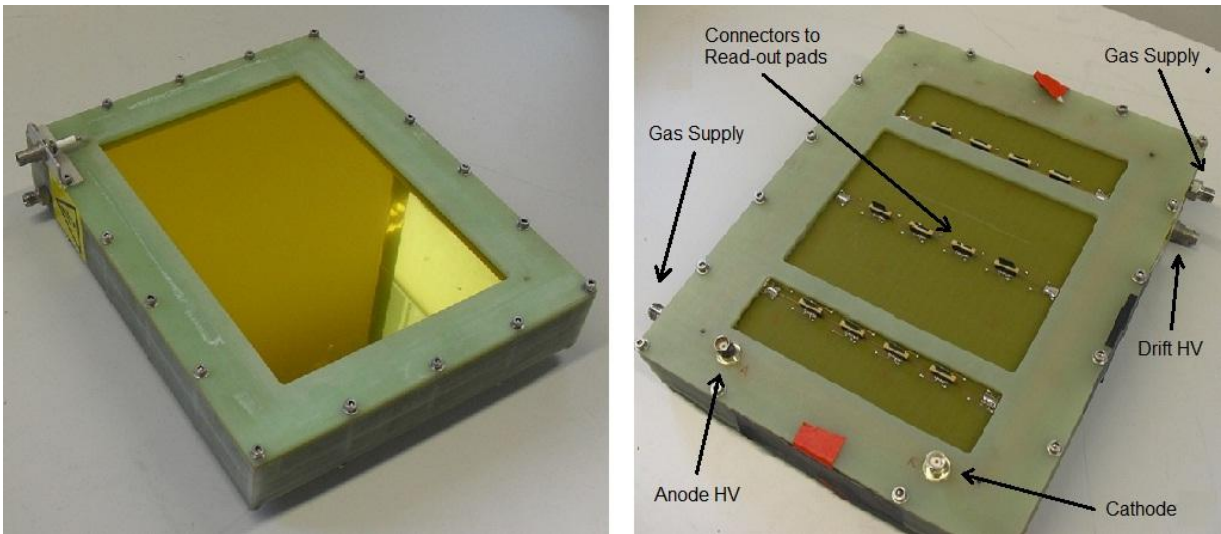
Figure 7.1: Pictures of the TRD chamber used in the project. left.: chamber front side with the entrance window for particles. A radiator can be attached on top of the entrance window. right.: chamber back side with connectors to read-out pads. The chamber is 310 mm long, 250 mm wide and 57 mm thick

7.1. The TRD Prototype Chamber

Compared to the actual TRD chambers used in ALICE, the TRD Prototype chamber used in this project shows some differences. The first difference is in size. The prototype chamber is 310 mm long, 250 mm wide and 57 mm thick. The TRD chambers used in ALICE are bigger: depending on the position of a chamber in a supermodule, the modules used in ALICE are 1100 mm to 1605 mm long in beam direction, 956 mm

to 1178 mm wide and 105 mm thick. The differences in length and width are due to the fact that the chambers used in ALICE are supposed to cover a large area, which is not necessary for this prototype. The difference in thickness derives from the fact that the prototype chamber does not have a radiator attached to its front side. So for this experiment, no transition radiation is observed. A radiator can be attached in front of the entrance window of the chamber. The readout chamber of the prototype has the same dimensions as the readout chamber of the TRDs used in ALICE. The wire geometry is also the same. The drift region of this prototype chamber is not outfitted with a chain of voltage deviders, connected to further drift electrodes on the inside faces. The readout pads are of the same dimensions ($7.25 \cdot 87.5$ mm^2), but due to its smaller size, the prototype chamber has got far fewer readout pads than the chambers used in ALICE, which have got 2304 pads, segmented into 16 pad rows and 144 pad columns. The prototype chamber has got 66 pads, segmented into 3 pad rows and 22 pad columns.

7.2. The Gas Supply

The TRD chamber has to be supplied with gas, as explained in Cha. 4.2. The gas enables high drift velocities in the drift region and a high amplification of ionisation in the amplification region of the MWPC. Another factor is a high quenching of photons emitted during secondary ionisation of the gas. In a transition radiation detector, there also has to be a high absorption for TR photons in the drift region. The gas mixture used in the TRD at ALICE - a mixture of xenon - carbon dioxide with a ratio of 85% to 15% - fulfils these requirements. Xenon has a relatively low absorption length of between 4 mm and 10 mm of TR photons with energies in the soft x-ray region, as shown in Fig. 7.2. Adding a component of carbon dioxide to xenon increases the drift velocity v_D and reduces the gas gain [19]. Carbon dioxide shows good absorption qualities of photons over a wide range of energies. It is suitable as a quencher gas.

For the experiment here, another consideration has to be taken into account. The gas system is not closed. We constantly supply the chamber with fresh gas. Waste gas is dumped through an outlet. Xenon is too expensive for such a set-up. The next best gas to use, when considering TR photon absorption, would be Krypton, which is also too expensive. Thus Argon is used in the experiment here. The downside of using Argon is its high absorption length of TR photons of approximately 10 mm to 100 mm. The chamber's drift region is 30 mm long; as a result, most of the TR photons would leave the chamber without being absorbed by the gas. For this experiment, good absorption qualities of TR photons are not need, because there is no radiator in which they are produced. The other requirements - high drift velocity and gas gain - can be fulfilled with Argon as well by adjusting the voltages applied to the chamber's electrodes [18]. For the experiment, a mixture of Argon - Carbon Dioxide with a ratio of 70 % to 30 % is used.
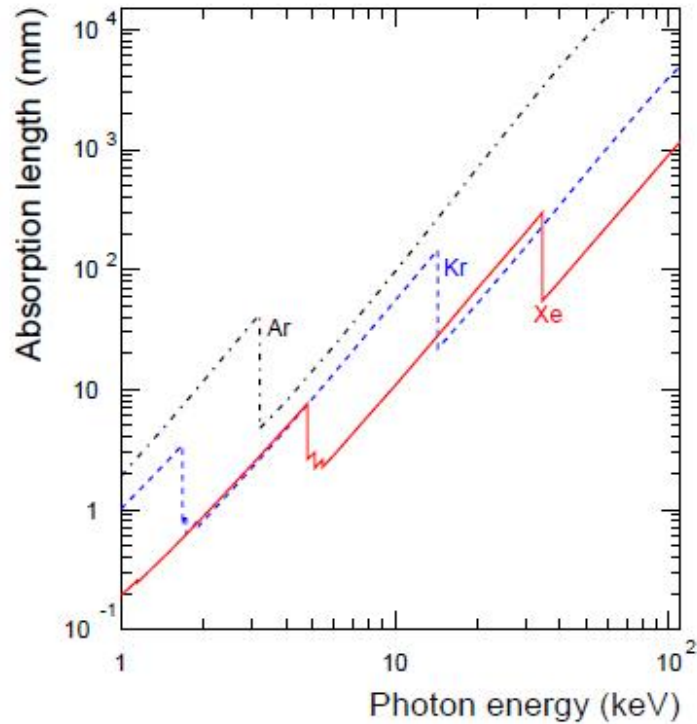
Figure 7.2: X-ray absorption length in different noble gases [2]

The TRD chamber is supplied with with gas via a supply system, as illustrated in Fig. 7.3 , which consists of a flow regulator, a bubbler, polyethylene pipes, and optionally a gas chromatograph. Before the gas from the gas cylinder is piped through the TRD it flows through a flow regulator, with which the gas flow can be regulated. Before leaving the system through an outlet, the gas flows through a gas bubbler; its purpose is to create a small overpressure - here 0.5 mbar - in the system and thus protect the system from contamination by air. A gas chromatograph, an Orbissphere© oxygen analyser, is used to measure the contamination of the gas system with oxygen. Electronegative gases, e.g. oxygen, modify the drift properties due to electron capture, i.e. attachment [18]. As a result, a fraction of the electrons drifting towards the MWPC are absorbed and the strength of the signals induced on the read-out pads becomes smaller. Even oxygen levels of a few ppm (parts per million) significantly reduce the registered pulse heights. The TRD chambers at ALICE are operated with oxygen contaminations below 10 ppm [17]. To achieve such low levels of contamination requires an ultra tight gas system. For our set-up, such low levels of oxygen contamination were not achieved, even though an Argon sniffer was used to find leaks in the chamber. The lowest achieved oxygen content was 30 ppm at a flow of fresh gas of 12 l/h.
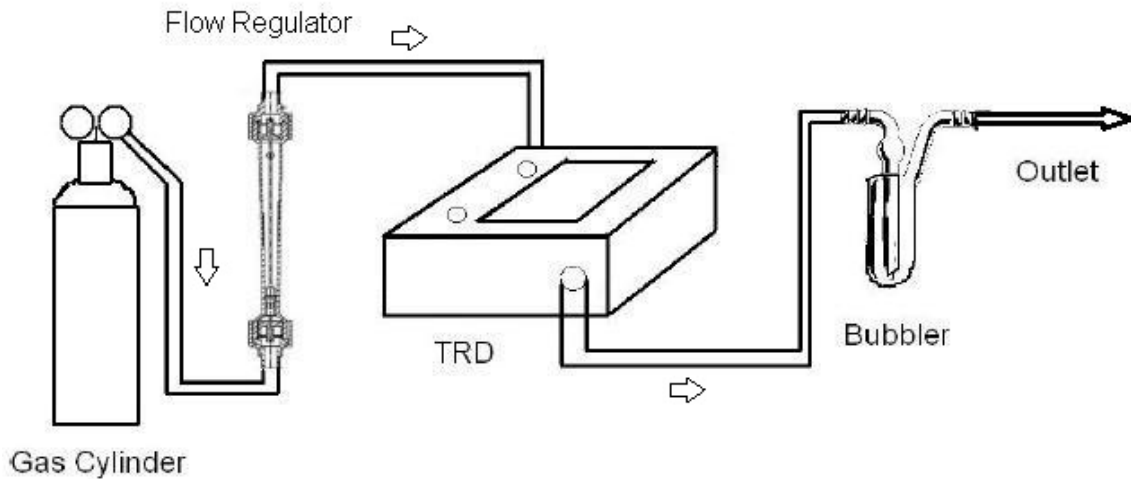
Figure 7.3: Schematic representation of the gas supply system used in the set-up

7.3. The High Voltage Supply

The drift electrode is supplied with negative high voltage, while the anode wires are supplied with positive high voltage; the cathode wires as well as the pad plane are grounded, as shown in Fig. 7.4. Fig. 7.5 shows three pictures of the inside of the TRD chamber. On the upper left side, there is a picture of the frontside of the chamber with the drift electrode (silver mylar foil). The mylar foil is connected to one of the high voltage connectors. The picture on the upper right side of Fig. 7.5 shows one of the inner sides of the drift chamber. The drift region of this prototype chamber is not outfitted with a chain of voltage dividers, connected to further drift electrodes on the inside faces. The decrease in voltage, and thus in the electric field, in the drift region is thus not uniform close to the inner sides. The third picture in Fig. 7.5 shows the backside of the chamber. There are three columns of 22 rows of read-out pads, which are printed circuit boards (PCB) with a layer of copper. In front of them are the anode and cathode wires; the anode wires are connected to the high voltage connector (lower connector) and the cathode wires are connected to the BNC connector (upper connector).
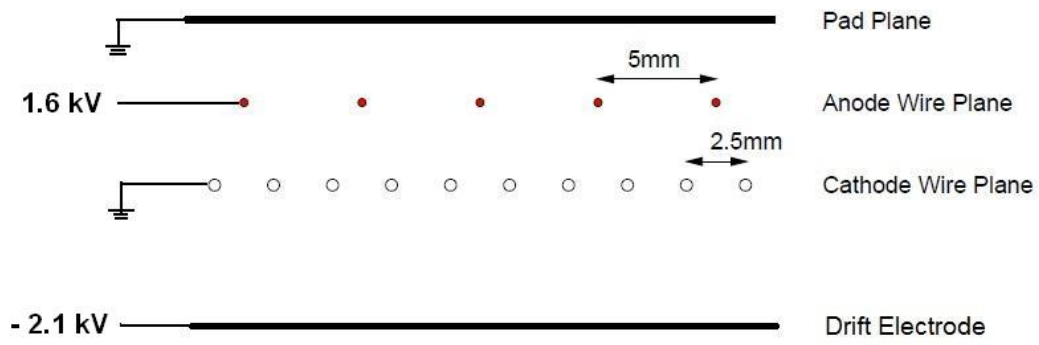
Figure 7.4: Schematic view of the high voltage supply of the ALICE TRD read-out chamber. The distance between the drift electrode and the anode wires is 37 mm. The distance between the anode wires and cathode wires as well as the anode wires and the pad plane is 3.5 mm (adapted from [2])
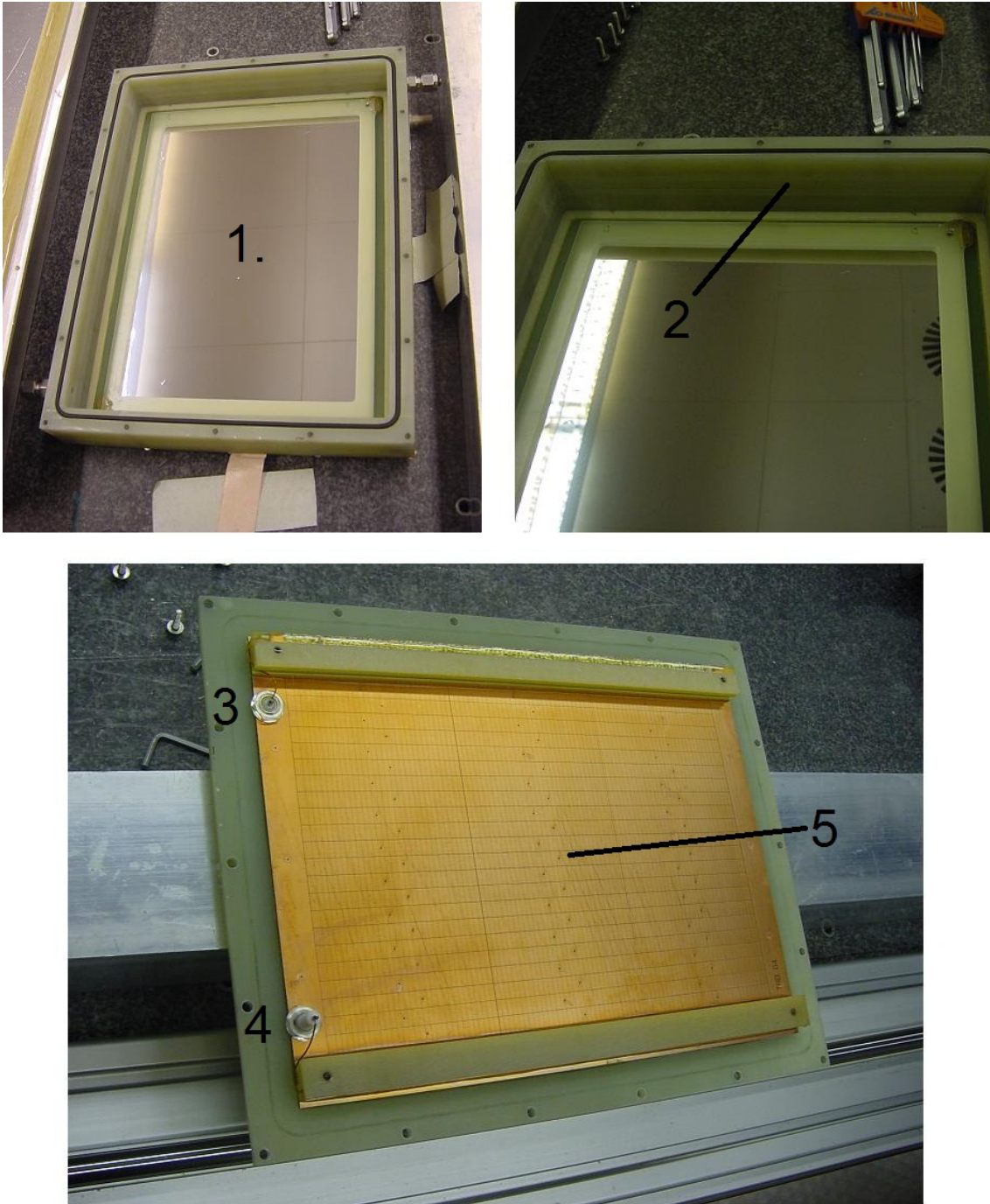
Figure 7.5: Inner view of the TRD prototype chamber. upper left:front side with drift electrode, silver mylar foil (1). upper right: side face (2) without further drift electrodes). lower: back side with cathode connector (3), anode HV connector (4) and cathode/anode wires above read-out pads (5). The chamber is 310 mm long, 250 mm wide and 57 mm thick

The next step in commissioning the TRD chamber is to make a first check whether the electric circuitry of the chamber is operational. High voltage is applied to the drift electrode and the anode wires. The resistance of the mylar foil and the wires is negligibly small and the drift region is not outfitted with a voltage divider chain. The procedure for testing the circuitry encompasses ramping to some voltage, keeping it there for some time and then ramping it down. This is done for both drift electrode and anode. While ramping to some voltage, small charging currents might be observed. These charging currents should be below 1 nA, if the ramping is done slowly (10 V/s). While keeping the voltage at some value, these currents should subside, if the electric circuitry of the chamber is undamaged. If the electronic circuitry is damaged, e.g. by broken wires and a resultant short circuit, there will be a sharp rise in the current while increasing the applied voltage.

Guide values for possible voltages applied to the drift electrode and the anode wires are needed to carry out the test. Drift velocities of electrons in the drift region and amplification factors in the amplification region depend on the applied voltages. Feasible values for drift velocities are in the region of 1.5 $\frac{cm}{\mu s}$ and 2 $\frac{cm}{\mu s}$ and the amplification factor, the gain, should be between 10^3 and 10^4. Working voltages for this specific gas mixture and wire configuration should be the following [18]: -2.1 kV for the drift electrode and +1.60 kV for the anode wires. The maximum resolution for the current of the high voltage power supply used in the experiment is 1 μA. Ramping up the voltages is first conducted with the chamber supplied with pure carbon dioxide. For carbon dioxide, the gas gain for the anode voltages used in the experiment is negligibly small. While ramping the voltages up to the guide values, the measured currents stayed below the resolution of the power supply of 1 μA. The chamber was now supplied with argon - carbon dioxide. Again the currents stayed below 1 μA. To really make certain that the electronic circuitry of the chamber and the connections to the pads are functioning properly is only possible when the data from the individual pads are read out.

7.4. The Mechanical Installation

The mechanical installation consists of a rack serving as a main support structure and of holders supporting the individual components: the scintillator assemblies and the TRD prototype module. Fig. 7.6 shows technical drawings of the support structure. Two scintillators are mounted above the TRD module and two scintillators are mounted below the TRD module. The scintillators in each level are arranged perpendicular to each other. Their overlapping area is just above - or below - the TRD module's active area. With the help of adjusting screws the position of each individual component can be adjusted. Furthermore, the scintillators can be turned in their sockets and thereby their overlapping area can be made smaller. The active area consists of 16 pads, with a total active area of $116 \cdot 87.5$ mm^2. The scintillators are slightly turned so that their overlapping area meets this active area. The main supporting structure is made of

item©ⓒ profiles. The individual supporting structures are made of aluminium. Fig. 7.7 shows the actual mechanical installation. The item©ⓒ profile (black rack) supports the individual support structures (aluminium) as well as parts of the gas supply system and the low voltage power supply for the readout board.
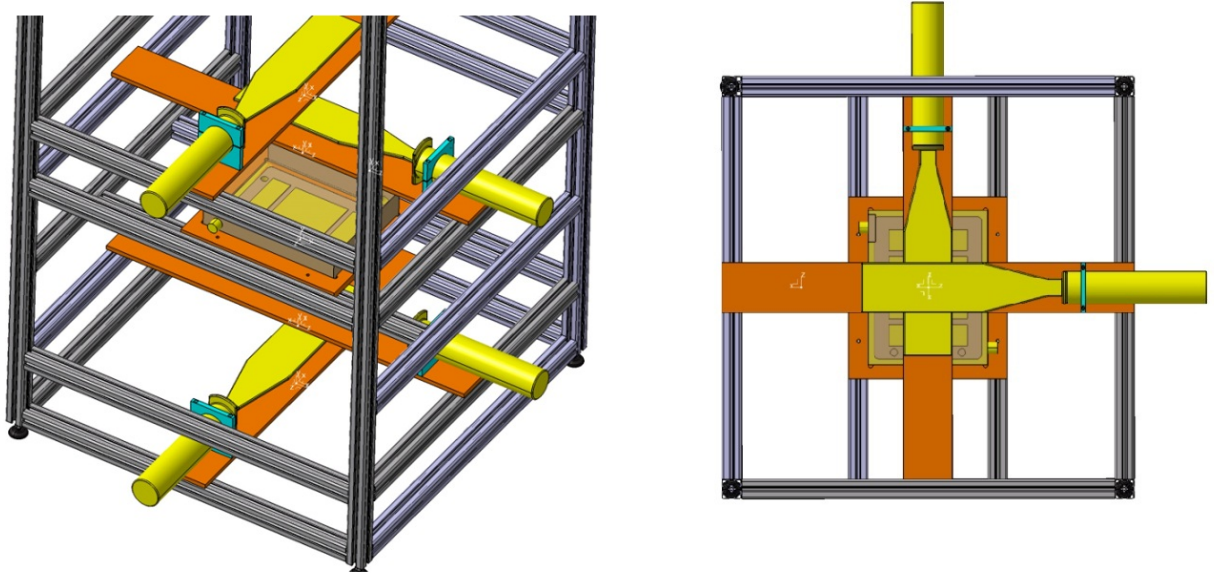
Figure 7.6: Technical drawings of the mechanical installation from different angles. The scintillators (yellow) are mounted on support structures (blue and orange). The scintillators are arranged perpendicular to each other. Their overlapping area matches the active area of the TRD chamber (brownish transparent box.). The mechanical installation is 1500 mm high and has a square footprint of 840 mm

Figure 7.7: Picture of the mechanical installation supporting the individual components. The main support structure (black) holds the support structures of the individual components (silver, aluminium), the four scintillators (black) and the TRD chamber (wrapped in aluminium foil)
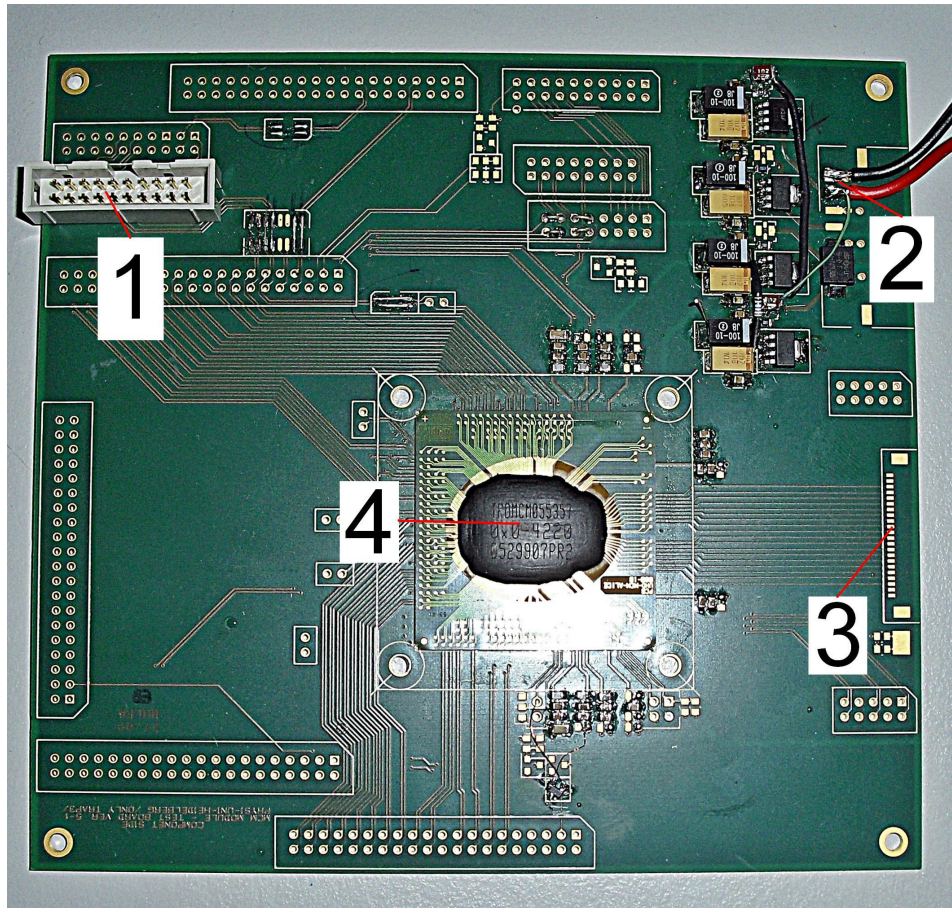
Figure 7.8: Picture of the read-out board (1) connector to USB adapter (2) low voltage power supply cable (3) connection to read-out pads (4) MCM. The read-out board is 19 cm long and 15 cm wide

8. Read-Out and Display of TRD data

8.1. Read-Out

The read-out system consists of an MCM ("Multi Chip Module"), as explained in Cha. 4.3, mounted on a read-out board which is connected to the read-out pads on the backside of the TRD chamber, and of a USB ("Universal Serial Bus") adapter managing the communication between the trigger set-up, the MCM and a computer. The USB adapter has been developed within this thesis.

The MCM used in this set-up comprises a PASA ("Pre-Amplifier and Shaper") and a TRAP ("Tracklet Processor") with an ADC ("Analogue to Digital Converter") and
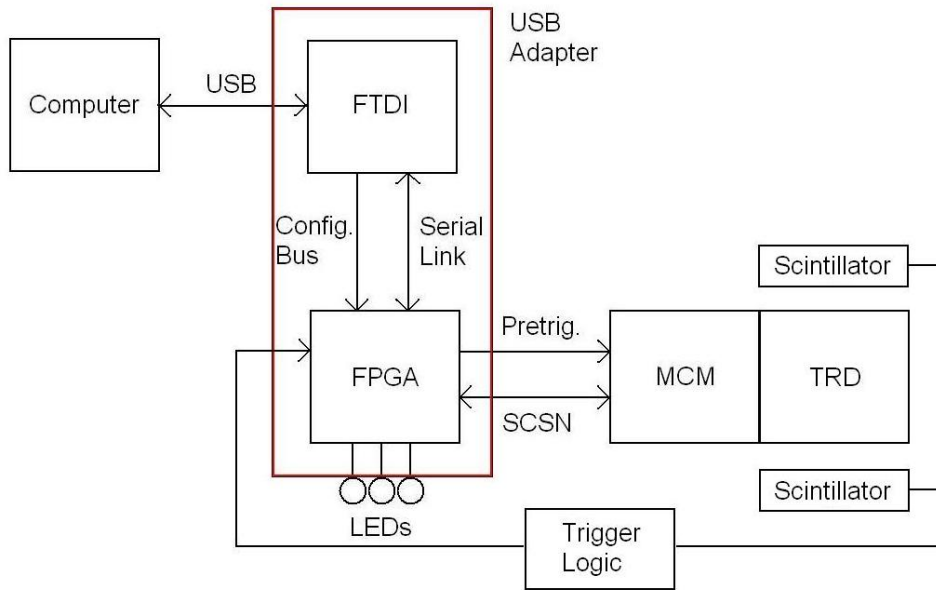
Figure 8.1: Schematic representation of the USB adapter for the read-out and its connection to the MCM, the computer and the trigger logic

an event buffer. It is mounted the read-out board, as shown in Fig. 7.8. The board is supplied with low voltage (≈ 5 V), a connection to the read-out pads and a connection to the USB adapter. 16 of the 18 charge sensitive inputs of the MCM are connected to the 16 pads in the middle of the centre pad column via a flat ribbon cable. The connection has to be as short as possible to minimise the effect of noise on the signal transmission (here ≈ 12 cm). The PASA amplifies the signals from the individual pads with a gain of 6.1 $\frac{mV}{fC}$. Additionally, if tail cancellation is enabled during the configuration of the MCM, the PASA shapes the signal to cancel its ion tail. The ADC digitises these analogue signals. The TRAP sets a baseline for the ADC values at an ADC value of 10. These data are stored in the event buffer.

The USB adapter consists of an FTDI chip and an FPGA (*Field Programmable Gate Array*). The FTDI chip allows the FPGA to be configured via USB and converts serial transmissions to USB signals and vice versa. The FPGA is responsible for the configuration of the MCM. It is used to implement the required interface logic, such as the SCSN protocol (*Slow Control Serial Network*). The MCM has an SCSN interface used for its configuration and programming; it also provides read-out of ADC data. The FPGA is responsible for distributing trigger information. It is thus responsible for data distribution and processing in the read-out system: it processes data from the trigger, the computer and the MCM. Three LEDs, a red, yellow and a green one, are connected to the FPGA. The red light flashes, when a trigger signal is received by the FPGA. The green light flashes, when the computer and the FPGA communicate and the yellow light flashes when the FPGA communicates with the MCM.

The read-out scheme is the following. The FPGA receives a trigger signal; the red light flashes. After an adjustable delay, the FPGA sends a pre-trigger to the TRAP; the yellow light flashes. An event is sampled with a rate of 10 MHz. The data from the individual pads are adjusted to a baseline of an ADC value of 10 and stored in the event buffer. The FPGA asks for the ADC data. The data consist of 32-bit words in which three sampled ADC values (10 bit/sample) have been packed. Two additional bits are used for data integrity checks. The data contain ADC values for 30 time bins for each of the 16 pads, i.e. 160 numbers. Via the FTDI chip, the PC asks the FPGA for the data; the green light flashes. The computer performs three bits shifts on each of the numbers: 2 bits, 10 bits and 10 bits. The ADC values are stored in an array. For each triggered event, the ADC values are dumped on the terminal. In parallel, the data are saved in a text file, in which the ADC values per pad are listed one value below the other and an empty line is inserted after each event, for further analysis and display.

8.2. Noise

The analogue signals induced on the pads are very small (10^5 to 10^6 positive ions). To limit the influence of noise, the cables connecting the MCM with the read-out pads is kept as short as possible. The influence of external electric fields, e.g. through currents in the photomultipliers and in the electronic modules of the trigger set-up, were observed as noise when reading out the ADC data. To limit the influence of external electric fields, and thereby minimise the influence of noise on the measurements, the chamber was wrapped in aluminium foil. The aluminium foil is grounded by connecting it to the ground connectors on the MCM. Fig 8.2 shows the measured distribution of noise of one read-out pad. A fit with a Gaussian function has been conducted. The mean of the distribution is at an ADC value of 10.35, which means 0.35 above the set baseline. The root mean square (rms) of the fitted distribution is 3.262. The distribution of noise is quite wide with ADC values up to 24. For the TRD chambers used in ALICE, the noise has an rms of approximately 1.0, which corresponds to 1000 electrons [2]. The high level of noise for this set-up results in a smaller signal-to-noise ratio compared to the TRDs used in ALICE, which can make it difficult to distinguish between signals due to ionising particles and noise.

8.3. Display of Data

The graphic display of data coming from the TRAP is done with the analysis tool ROOT [20]. Each time new ADC data are stored in the text file, the data are read out. A histogram is filled with the ADC values per pad and time bin, as shown in the upper figure in Fig. 8.3. There is a new histogram for each triggered event and thus an online event display.
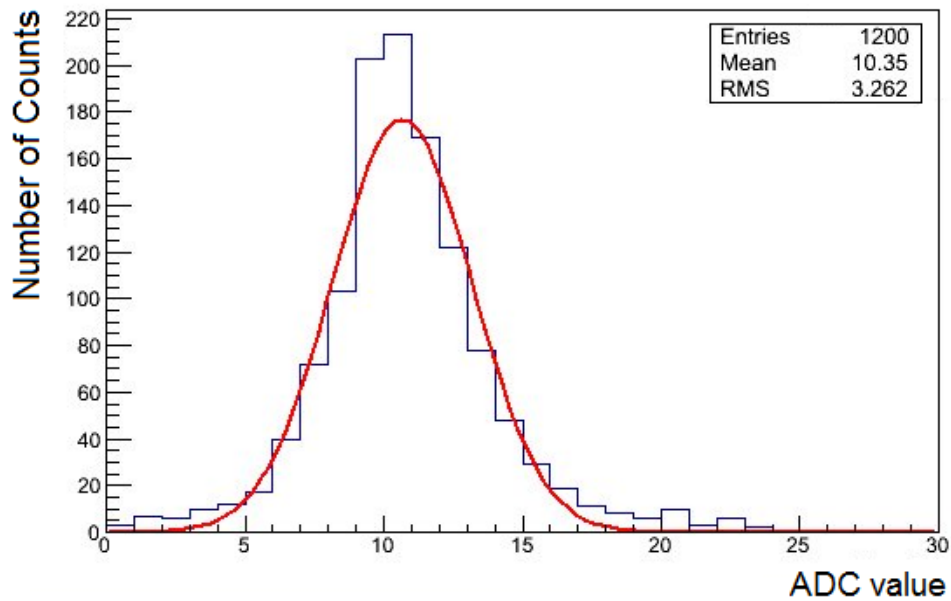
Figure 8.2: Distribution of noise of one read-out pad for 1200 ADC values fitted with a
Gaussian function

The upper figure in Fig. 8.3 shows a display of a triggered event. The histogram depicts the induced charge on each read-out pad per time bin. Later time bins belong to ionisation clusters produced at the beginning of the drift region. The ionisation cluster with its maximum in time bin 6 at pad 10 belongs to the ionisation in the amplification region. A detailled discussion of average heights of ionisation clusters can be found in Chapter 9. "Distributions of Average Pulse Heights".

8.4. Cluster Finding Algorithm and Fitting

A cluster finding algorithm analyses the ADC data of a triggered event and finds ionisation clusters. The baseline is not subtracted from the ADC values. The cluster finding algorithm works the following way. For each time bin, the algorithm finds the pad with the highest ADC value. If the highest ADC value is below 25, the algorithm identifies it as being due to noise and moves on to the next time bin. If the highest ADC value is above 25, i.e. above noise, the algorithm further analyses the ADC values of this time bin. The charge related to one cluster is not deposited on a single pad, but on at least three pads per time bin. The ADC value of the pad with the highest ADC value, ADC (y), is summed with the ADC values of its adjacent pads , ADC(x) and ADC(z). If this sum is bigger than an adjustable value, here a value of 44, a cluster is found. This further minimises the effect of noise on the cluster finding. The next step is to fix the clusters exact position. If y is the pad number with the highest ADC value and x and z are the positions of its adjacent pads, the position of the cluster in pad units is:

54

$$\text{position} = \frac{\text{ADC(x)} \cdot \text{x} + \text{ADC(y)} \cdot \text{y} + \text{ADC(z)} \cdot \text{z}}{\text{ADC(x)} + \text{ADC(y)} + \text{ADC(z)}}. \tag{8.1}$$

The algorithm analyses the ADC data of each time bin; it calculates the position of clusters in pad units and time bins. An ionisation cluster has a long ion tail. If the pulse height of a cluster is high enough, the signal the ion tail induces on the read-out pads is treated as a separate cluster. The found clusters are plotted, as shown in the lower figure in Fig. 8.3. A straight line fit through the found clusters is conducted. If the reduced chi-square of the fit is below $\chi^2 = 3$, the fitted line is plotted, as shown in the lower figure in Fig. 8.3. The result is a track of an ionising particle through the TRD chamber, i.e. a tracklet.

With more than one ionising particle passing through the TRD, as shown in the upper figure in Fig. 8.4, the cluster finding algorithm works. If there are more than one cluster per time bin, only the highest cluster is found and plotted, as shown in the lower figure in Fig. 8.4. The straight line fit is conducted with such events, but the reduced chi-square of the fitted line usually exceeds the condition $\chi^2 = 3$. The fitted line is therefore not plotted. Fig. 8.4 shows an event with more than one ionising particle passing through the TRD. The cluster at pad 4 and time bin 5 is most likely due to noise. It is not possible to deduce single tracks for this event on the basis of the event display. A possible interpretation would be that it is an event of a scattering of a low-energy particle.
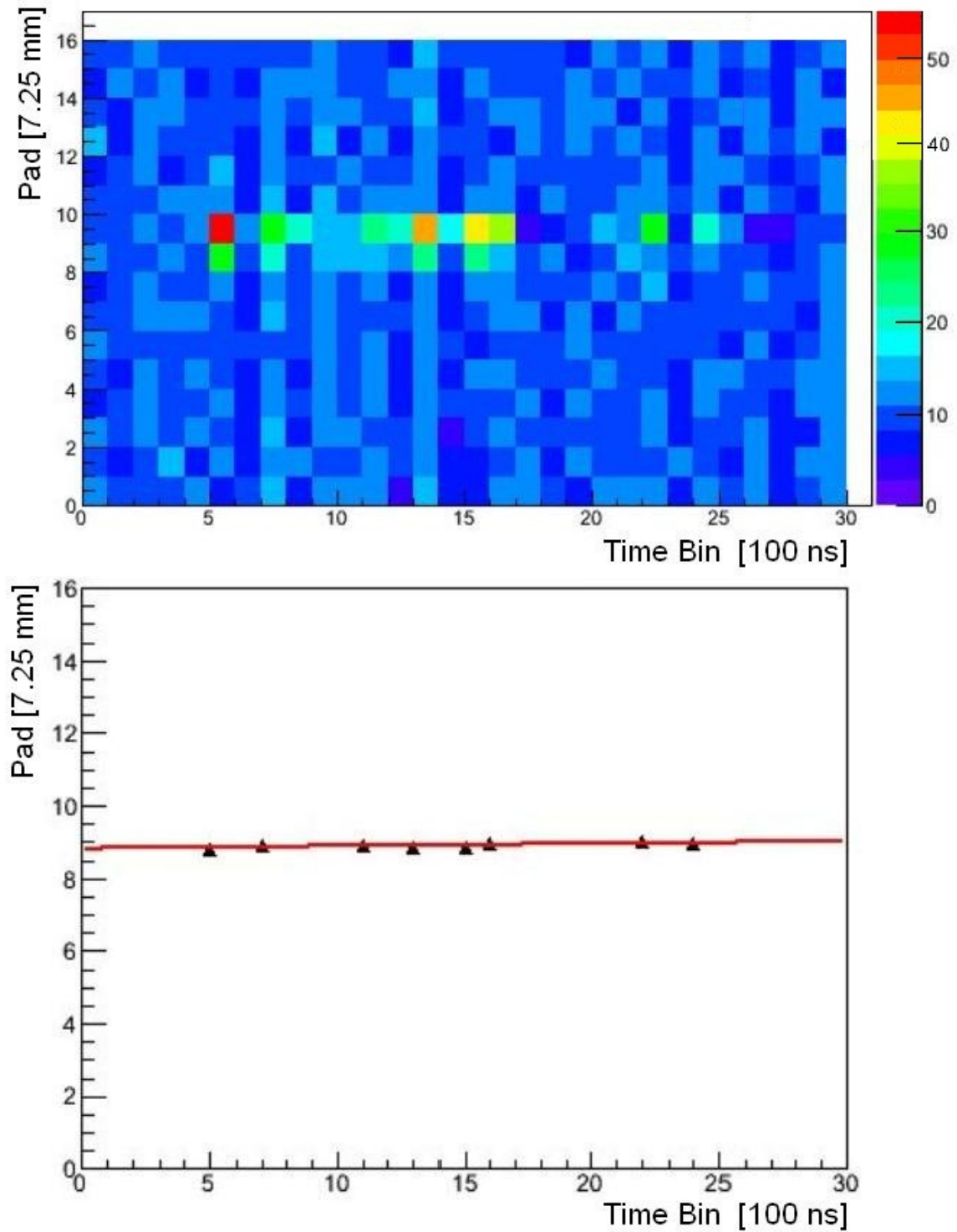
Figure 8.3: upper.: Display of a triggered event belonging to a single track of an ionising particle passing through the TRD (U_d = -2.1 kV; U_a = 1.635 kV). lower.: Straight line fit through found clusters

56
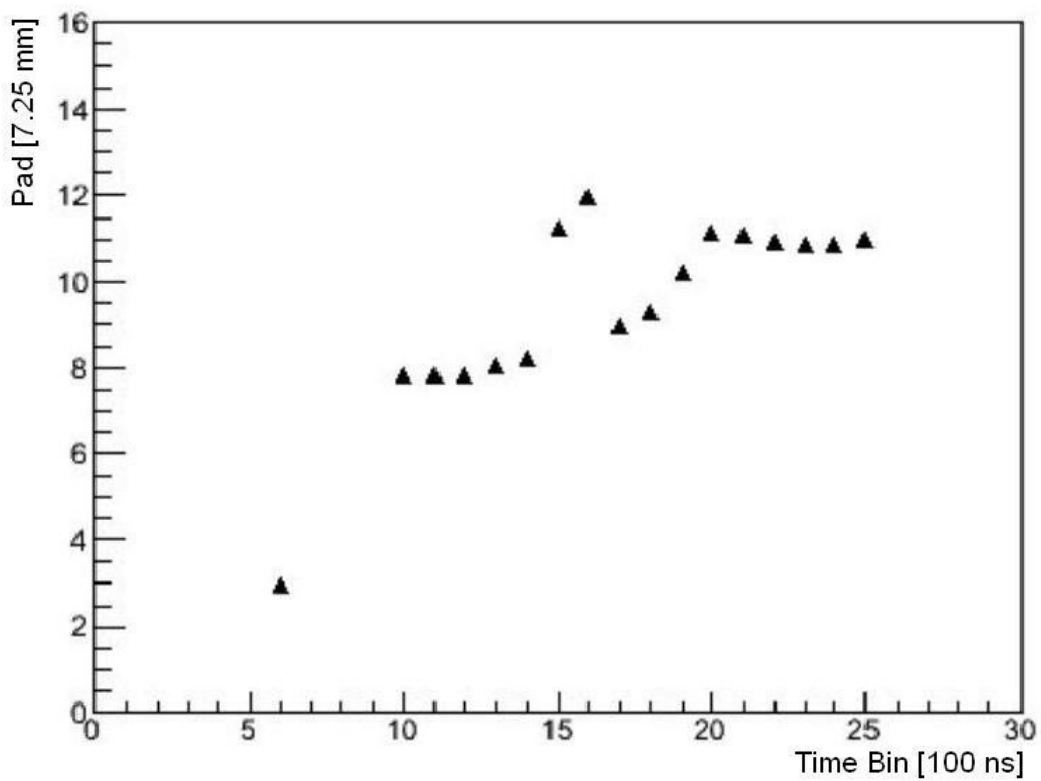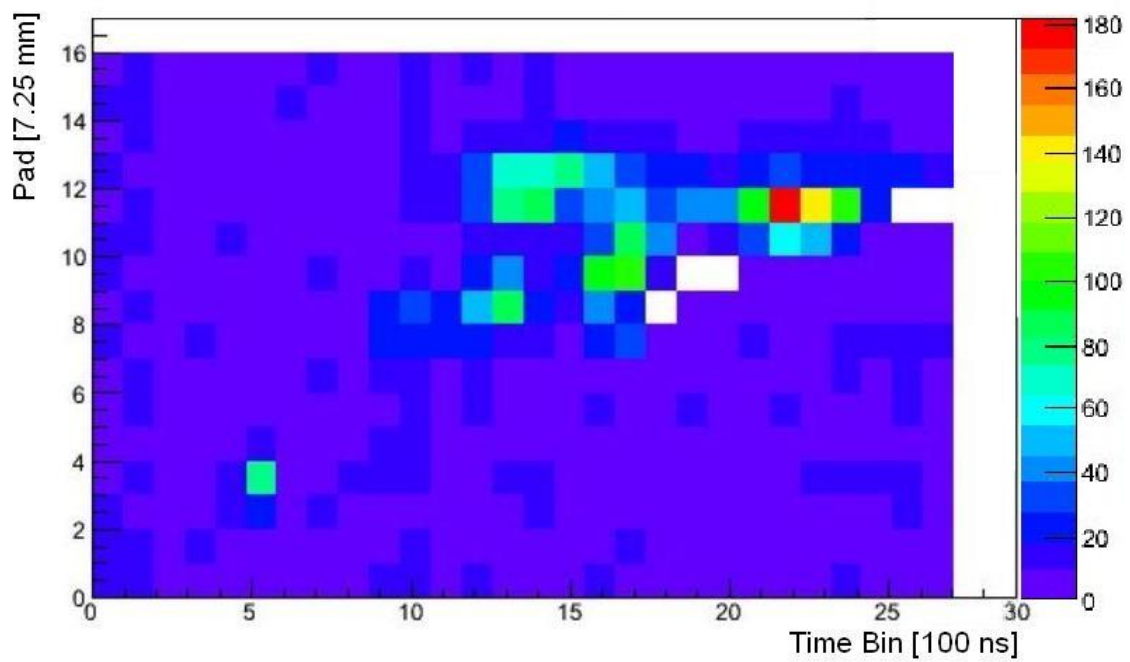
Figure 8.4: upper.: Display of a triggered event with more than one particle passing through the TRD (U_d = -2.1 kV; U_a = 1.635 kV). lower.: Found clusters belonging to an event with more than one particle passing trough the TRD

9. Distributions of Average Pulse Heights

Distributions of average pulse heights (APH) as a function of time bin were measured for different drift voltages and oxygen contents. The baseline of an ADC value of 10 was not deduced for these measurements. Approximately 3000 fitted events were recorded for each of the measurements. The summed pulse heights, the height of the found clusters normalised to the number of fitted events, per time bin were measured. Two series of measurements were conducted. For the first series, tail cancellation was enabled during the configuration of the MCM. For the second, it was disabled and the anode voltage was raised.
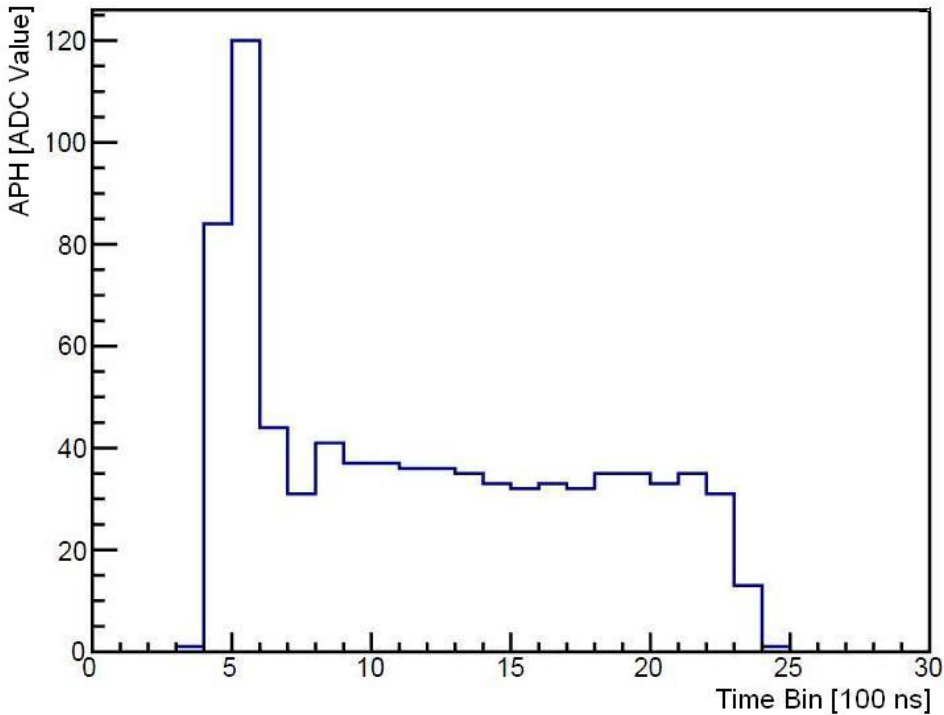
Figure 9.1: Distribution of average pulse heights (AHP) with tail cancellation enabled (U_d = -2.1 kV; U_a = 1.635 kV; 30 ppm oxygen content; Argon-Carbon Dioxide (70-30))

Fig. 9.1 shows the APH distribution for a drift voltage of U_d = -2.1 kV and 30 ppm oxygen content with tail cancellation enabled. The anode voltage was fixed at U_a = 1.635 kV for the first series of measurements of distributions of APH. The peak at the beginning of the distribution originates from the primary clusters in the amplification region, where ionisation from both sides of the anode wires contributes to the same time interval [2]. The plateau in the distribution from timebin 8 to timebin 23 is due to primary ionisations in the drift region. This plateau does not exhibit a small increase as

a function of drift time. There is a build-up of detector currents due to the ion tails of clusters, as shown in Fig. 4.6, because later clusters overlap with the ion tails of earlier clusters [2]. This build up would lead to such a small increase, but tail cancellation compensates for this build-up by adjusting the pulse heights of later clusters. For the ion tail of the peak, this leads to an over-compensation in time bin 7. For the plateau, the influence of the high noise levels can be seen. The plateau is usually approximately half as high as the peak [22]. The exact ratio depends on the ratio of the drift field to the field near the anode wires. For the set anode voltage, some ionisation clusters do not have enough signal strength to be distinguishable from noise. Thus the cluster finder does not find them. In total, this reduces the height of the plateau.

Fig. 9.2 shows the APH distribution for a drift voltage of $U_d = 0$ V and 30 ppm oxygen content with tail cancellation enabled. There was no drift of primary ionisation clusters in the drift region; therefore there is only the peak at the beginning from primary clusters in the amplification region. No ion tail can be observed due to tail cancellation. This measurement enables us to distinguish between the maximum due to primary ionisation in the amplification region and the plateau due to the electron drift.
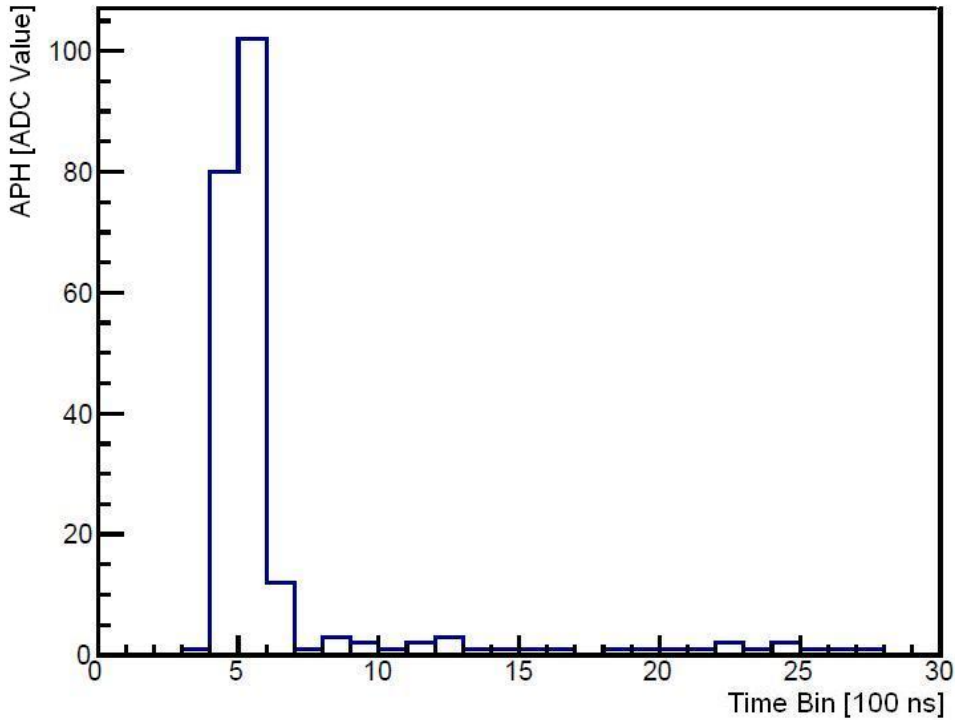
Figure 9.2: Distribution of APH with tail cancellation enabled ($U_d = 0$ kV; $U_a = 1.635$ kV; 30 ppm oxygen content; Argon-Carbon Dioxide (70-30))

Fig. 9.3 shows the APH distributions for different drift fields with tail cancellation enabled. For higher drift fields, the drift velocity of electrons in the drift region increases

and the plateau becomes narrower and higher. This is due to the compression of the same signal in shorter time intervals [2]. The drift velocity can be deduced from such distributions. The drift region is 30 mm long. The drift time of electrons for this distance is the width of the plateau. Due to uncertainties in delimiting the plateau from the amplification peak and uncertainties in deciding where the plateau ends, an error of one time bin is used for the width of the plateau. One time bin is also the maximum resolution with which drift times are measured with this set-up. The end of the drift plateau is estimated in the following way: the mid-height of the falling edge of the distribution is estimated as the end of the plateau. The beginning of the plateau is approximately in the middle of time bin 8. The drift velocity is calculated in the following way:

$$v_d = \frac{l_d}{w} \pm \frac{l_d \Delta w}{w^2} \tag{9.1}$$

where l_d is the length of the drift region, w is the width of the plateau and Δl_d is the error in measuring the width of the plateau. For a drift field of E_d = -0.63 kV/cm, the width of the plateau is 18 time bins; this yields a drift velocity of $v_d = (1.50 \pm 0.08)$ cm/μs. The measured drift velocities for different drift fields are the following:

- E_d = -0.63 kV/cm: $v_d = (1.50 \pm 0.08)$ cm/μs

- E_d = -0.70 kV/cm: $v_d = (1.67 \pm 0.09)$ cm/μs

- E_d = -0.73 kV/cm: $v_d = (1.77 \pm 0.10)$ cm/μs

These values are compatible with the measured data of Sauli and Preisert [21], shown in Appendix, Fig. A.8.
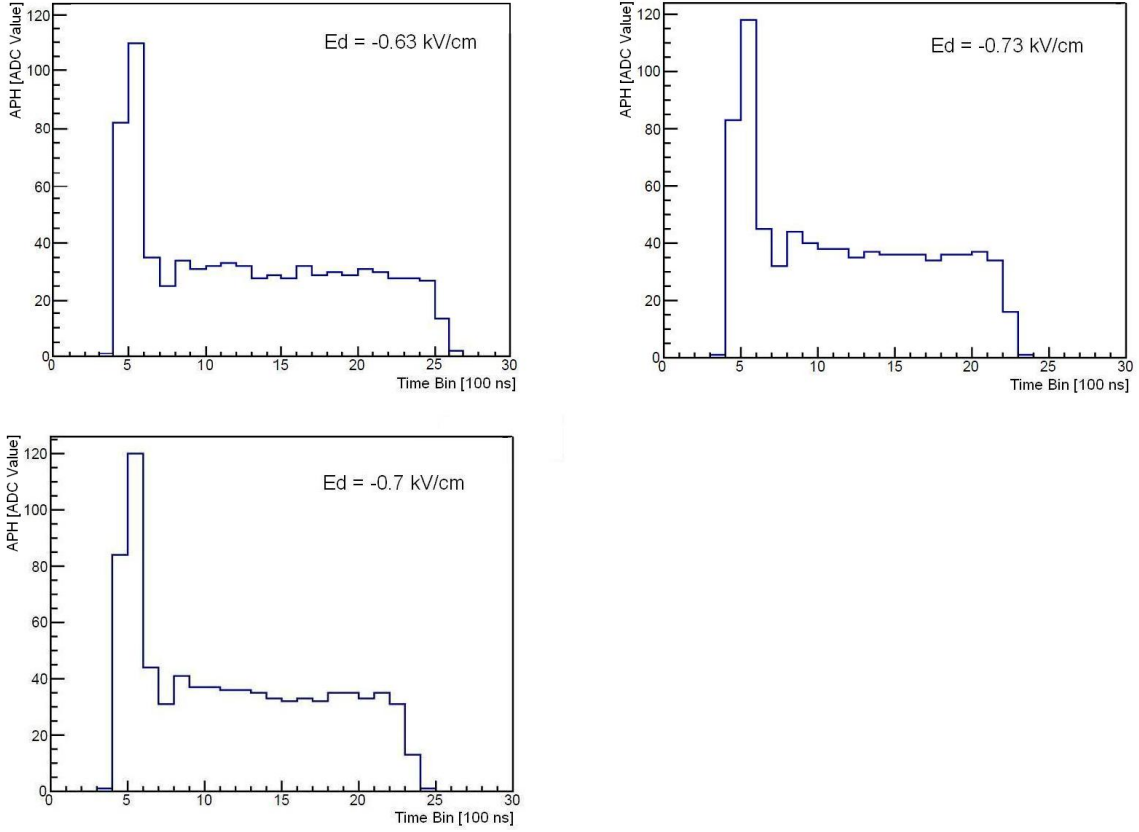
Figure 9.3: Average pulse height as a function of time bin for different drift fields with tail cancellation enabled ($U_a = 1.635$ kV; 30 ppm oxygen content; Argon-Carbon Dioxide (70-30))

Fig. 9.4 shows APH distributions different oxygen contents (30 ppm, 50 ppm, 70 ppm, 150 ppm). As explained in Chapter 7.2 "Gas Supply", a high level of oxygen leads to high attachement, i.e. high number of electrons being captured by oxygen on their way through the drift region. The signal in the amplification region, where electron drift is little, is affected to a much smaller extend than the signals in the plateau. In case of attachment, the number of electrons decreases as a function of drift time. The decrease observed here in Fig. 9.4 is stronger than excepted. The strong decrease observed for an oxygen content of 150 ppm would be expected for an oxygen content of approximately 400 ppm [22]. The observed decrease can thus be not only due to attachment. It is due to a combination of noise, the cluster finding algorithm and attachment. For higher oxygen contents, the signal strength of clusters for higher drift times decreases to such an extend that clusters are often not distinguishable from noise. The cluster finding algorithm does not find these clusters. This additionally reduces the APH for later time bins.
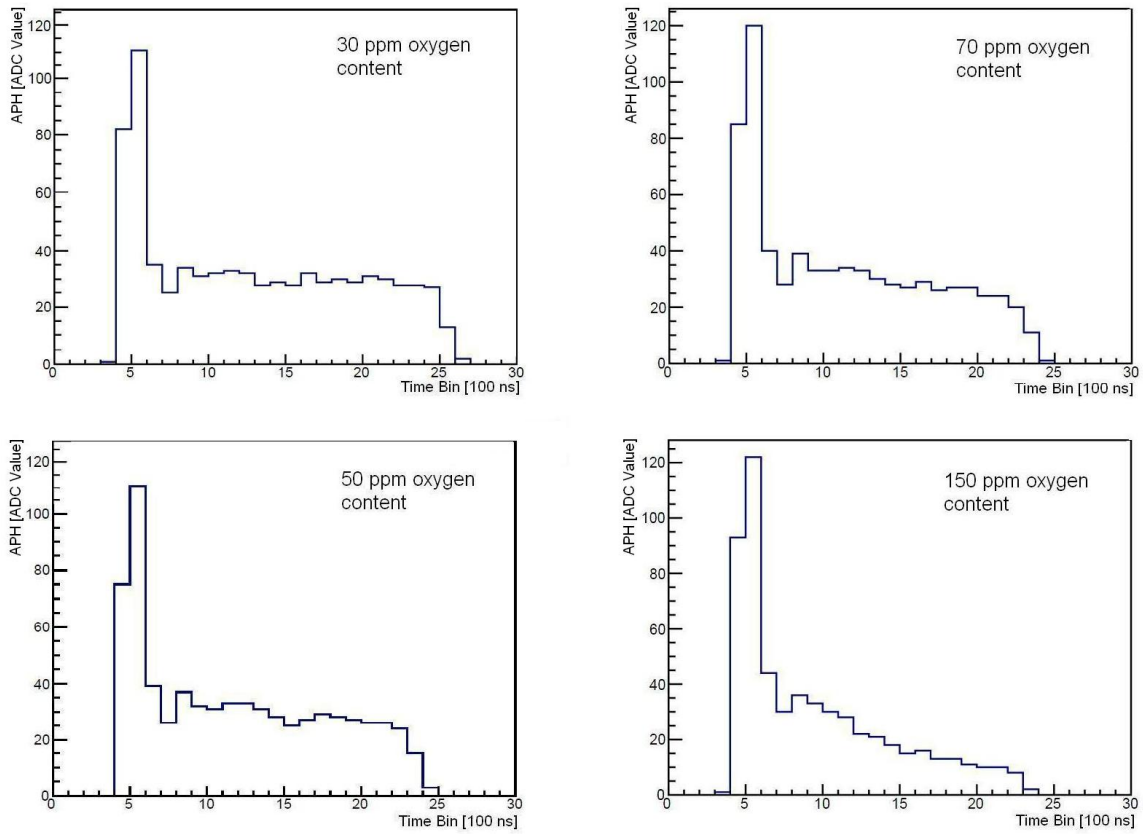
Figure 9.4: Average pulse height as a function of time bin for different oxygen contents with tail cancellation enabled (U_a = 1.635 kV; U_d = -2.1 kV)

For the second series of measurements, tail cancellation was disabled and the anode voltage was raised from $U_a = 1.635$ kV to $U_a = 1.7$ kV. Fig. 9.5 shows the APH distribution for a drift voltage of $U_d = 2.1$ kV and 30 ppm oxygen content with tail cancellation disabled. The higher anode voltage results in a higher gas gain. A raise in the anode voltage of 65 V results approximately in a doubling of the gas gain, according to data taken by A. Andronic *et al* [24]. The peak at early time bins has twice the height for an anode voltage of $U_a = 1.7$ kV than for $U_a = 1.635$ kV. For $U_a = 1.7$ kV, all clusters along the electron drift are found by the cluster finder and contribute to the distribution of APH. This explains why the plateau for $U_a = 1.7$ kV is more than twice as high than for $U_a = 1.635$ kV. Tail cancellation was disabled for this measurement. The distribution shows a small increase as a function of drift time, which is due to the build-up of detector currents. The overlap of the ion tails of the last clusters can also be observed.
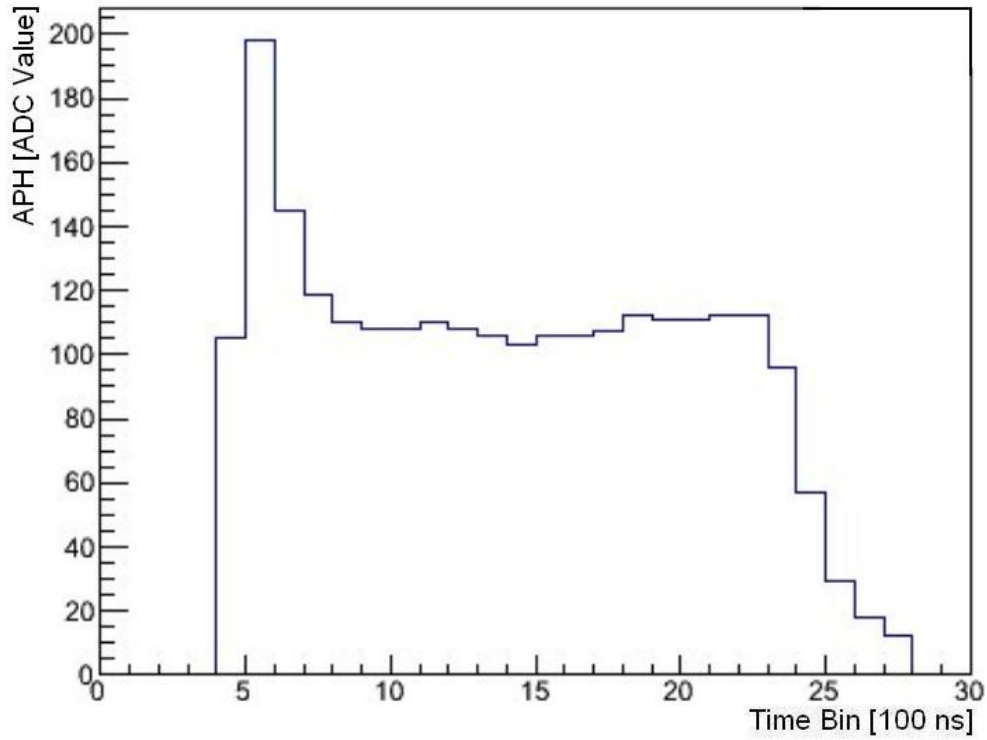
Figure 9.5: Distribution of APH with tail cancellation disabled (U_d = -2.1 kV; U_a = 1.7 kV; 30 ppm oxygen content; Argon-Carbon Dioxide (70-30))

Fig. 9.6 shows the APH distribution for a drift voltage of $U_d = 0$ kV and 30 ppm oxygen content with tail cancellation disabled. The long ion tail of approximately 600 ns can be observed.
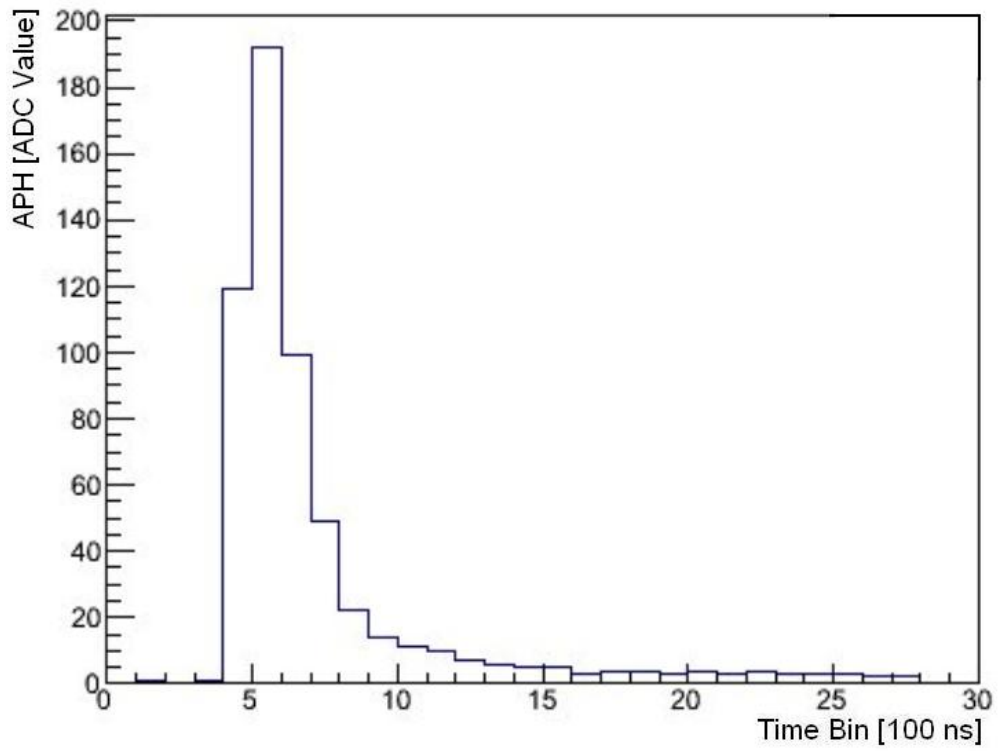
Figure 9.6: Distribution of APH with tail cancellation disabled (U_d = 0 kV; U_a = 1.7 kV; 30 ppm oxygen content; Argon-Carbon Dioxide (70-30))

10. Conclusion

The commissioning of the prototype TRD chamber included setting up a trigger for cosmic particles, supplying the chamber with gas, an $ArCO_2$ (70:30) mixture, and high voltage, setting up a read-out system of TRD data and the creation of a real-time event and track display. The components of the trigger set-up have been commissioned. Each time a cosmic particle passes through the active area of the TRD a trigger signal is sent. The electric circuitry of the chamber has been tested and found undamaged. The individual components have been mounted on a mechanical installation, which on the one hand supports them. On the other hand, the mechanical installation consists of movable elements, which makes a mechanical re-adjustment of the components possible. A read-out system, consisting of an MCM on a read-out board and a USB adapter for the communication between trigger, MCM and computer, has been implemented. The USB-adapter has been developed within this thesis. A trigger signal leads to a read-out of the data on the buffer in the MCM. The data is sent via the USB adapter to the computer, where it is analysed. A real-time graphic event display and a real-time display of fitted tracks have been created. Now it is possible to observe particle tracks in the TRD on a computer display in real-time.

Several key measurements have been carried out in order to study the performance of the chamber in detail. It has been studied how different drift voltages, anode voltages, and oxygen contents, as well as enabled and disabled tail cancellation influences the performance of the TRD chamber. Average pulse height distributions as a function of drift time have been recorded for different settings. The dependency of the drift velocity on the strength of the drift field and the influence of oxygen contamination on the signals have been measured. The data for the drift velocities are compatible with data taken by Sauli and Preisert [21]. The influence of electron attachment by oxygen atoms on signals has been observed. For high oxygen contents, attachments leads to a decrease in signal strength for higher drift times. The effect of the anode voltage on the signal gain has been observed. The measurements are compatible with data taken by A. Andronic et al [24]. The effect of an enabled tail cancellation filter in the read-out chip has been examined.

In several points, the performance of this prototype TRD chamber can be improved. One limiting factor on the performance is the high level of noise in the read-out system. The signal-to-noise ratio for the set-up is low compared to the TRDs used in ALICE. Lower noise levels would increase the performance of the cluster finding algorithm and thus the performance of the real-time track display. A solution for the high noise levels might be to come up with a shorter connection between the read-out pads and the PASA. This connection is the part of the front-end electronics which is the most susceptible to external electric fields. Another limiting factor is the high oxygen contamination in the chamber. The TRD chambers used in ALICE are operated with an oxygen content of below 10 ppm. In this set-up, the lowest achieved oxygen content was 30 ppm. Even

though an Argon sniffer was used, no leaks in the chamber were found. It would be easier to find leaks if the chamber was supplied with a lighter gas, e.g. helium. Another remedy for the high contamination with oxygen would be to use pipes with a higher quality than polyethylene pipes. This would lead to a tighter gas system. If these two limiting factors, noise and oxygen content were brought under control, the prototype TRD chamber could be used for more precise measurements of parameters interesting for the operation of TRDs: drift velocity, amplification gain, position resolution, attachment coefficients. If a closed-loop gas system were set up, the chamber could be supplied with $XeCO_2$. Absorption of transition radiation could then be observed, if a radiator were implemented in the set-up.

The present set-up allows for easy-to-use applications like testing new software and hardware components. The set-up also allows new members of the ALICE collaborations to become acquainted with the complex technology of the ALICE TRD. In the future, its compact design together with the graphical display would be ideally suited for exhibitions to demonstrate ALICE technology to a public audience, like the exhibition "Weltmaschine".

A. Appendix

A.1. Acronyms and Technical Terms

ADC   Analogue-to-Digital Converter
ALICE   A Large Ion Collider Experiment
APH   Average Pulse Height
ATLAS   A Toroidal LHC Apparatus
CERN   Conseil Europen pour la Recherche Nuclaire
CMS   Compact Muon Solenoid
CTP   Central Trigger Processor
FEE   Front-End Electronics
FTDI   Future Technology Devices International
GTU   Global Tracking Unit
ITS   Inner Tracking System
LHC   Large Hadron Collider
LHCb   Large Hadron Collider Beauty
MCM   Multi Chip Module
NIM   Nuclear Instrument Module
PASA   Pre-Amplifier and Shaper
PHOS   Photon Spectrometer
QGP   Quark Gluon Plasma
TOF   Time of Flight Detector
TPC   Time Projection Chamber
TRAP   Tracklet Processor
TRD   Transition Radiation Detector
USB   Universal Serial Bus

A.2. Scintillator Assemblies: Plateau Measurements
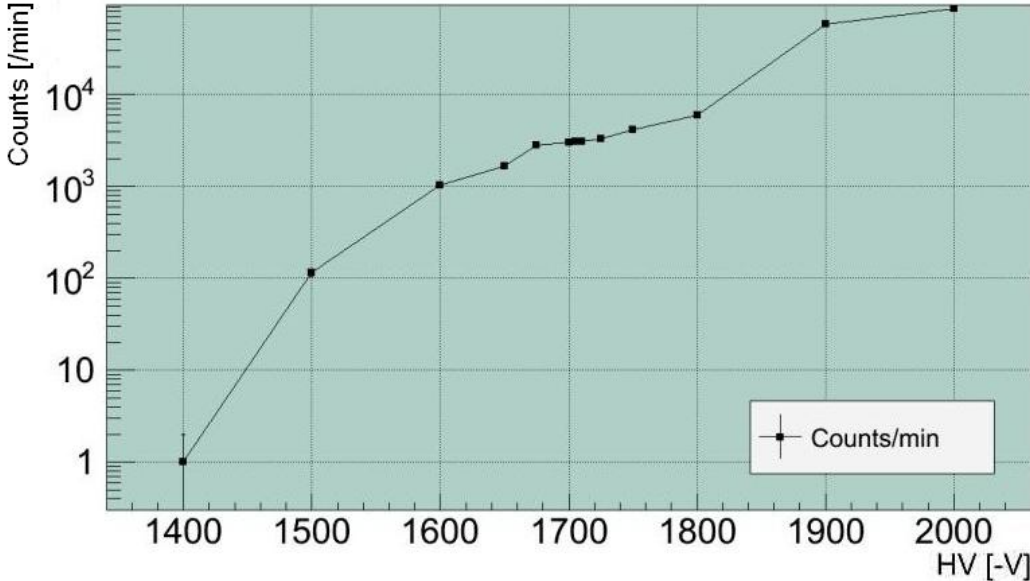
Figure A.1: Plateau Measurement for scintiallator PMT-01
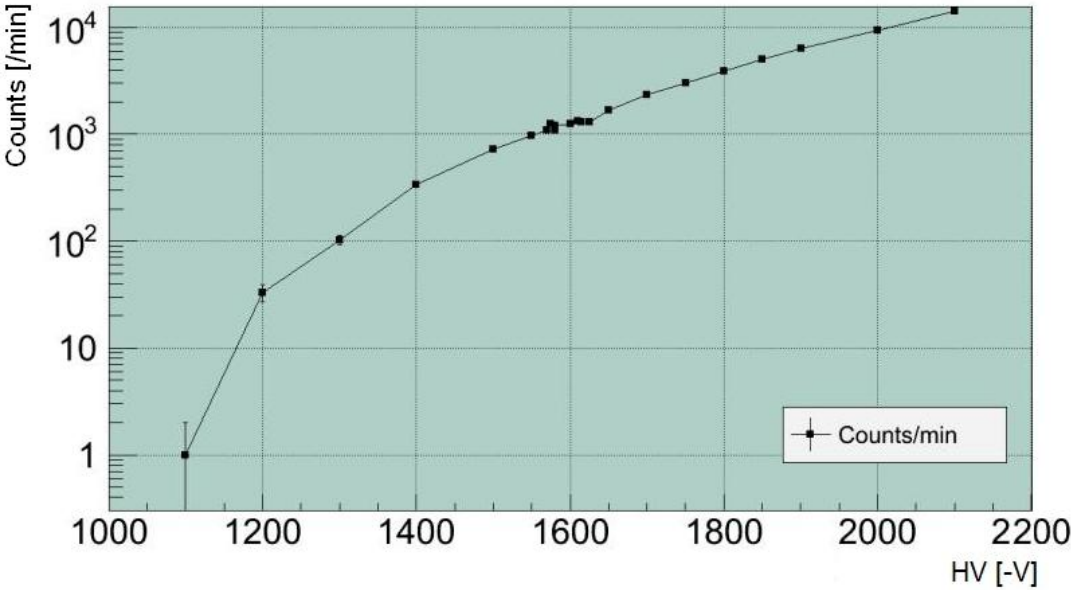
Figure A.2: Plateau Measurement for scintiallator PMT-02
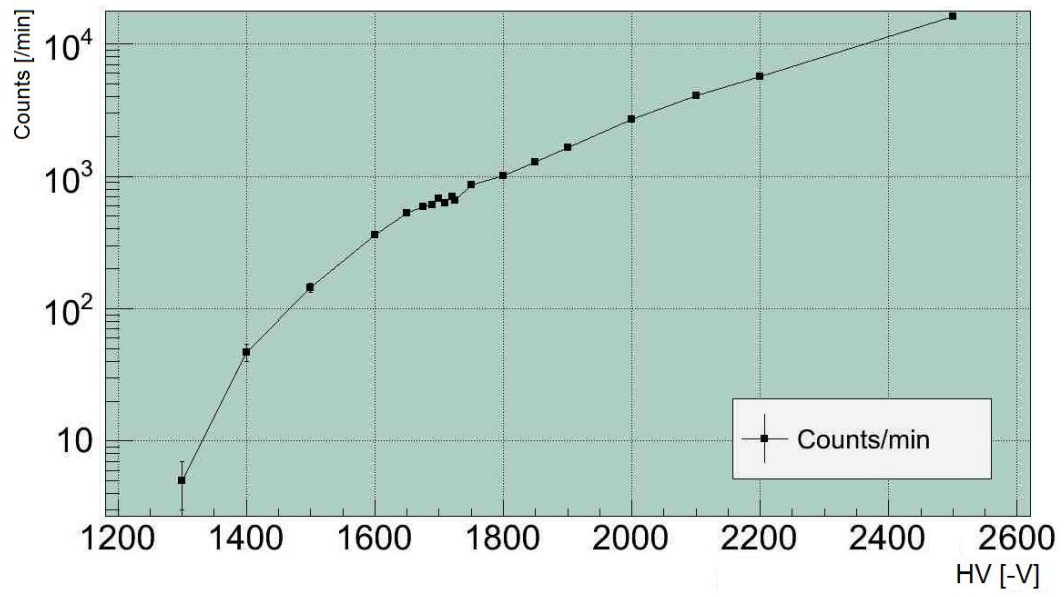
Figure A.3: Plateau Measurement for scintiallator PMT-04

A.3. Scintillator Assemblies: Adjusting Treshold Voltages
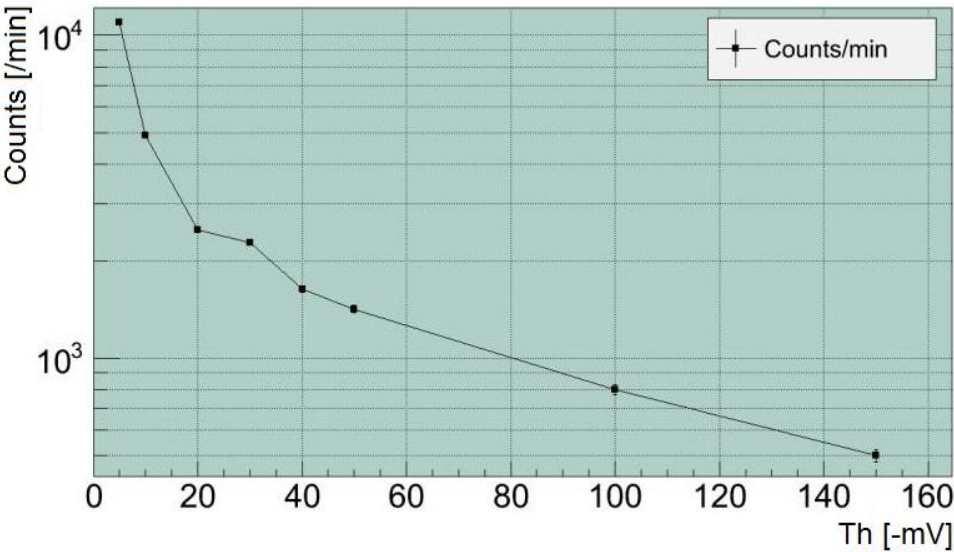
Figure A.4: Adjusting the discriminator threshold for scintillator PMT-01: measuring the count rate as a function of the discriminator threshold
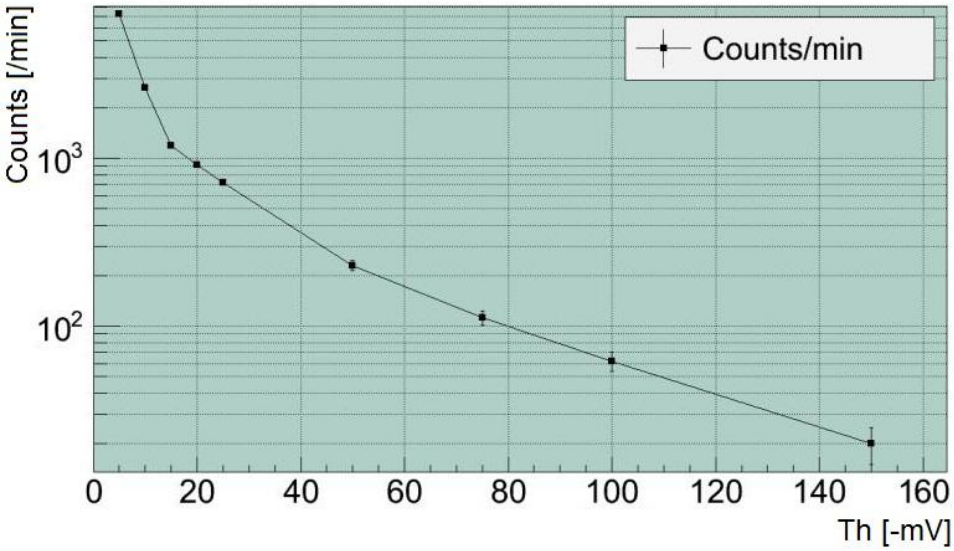
Figure A.5: Adjusting the discriminator threshold for scintillator PMT-02: measuring the count rate as a function of the discriminator threshold
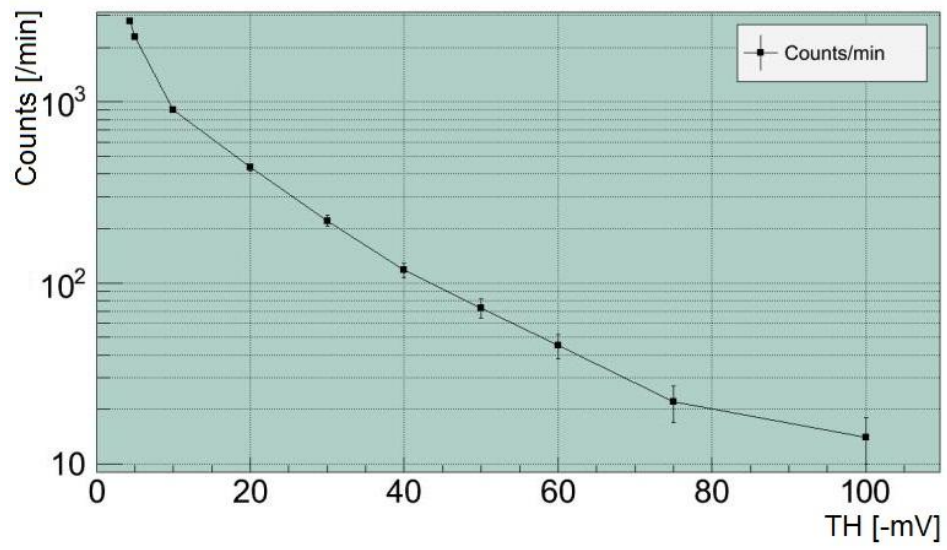
Figure A.6: Adjusting the discriminator threshold for scintillator PMT-04: measuring the count rate as a function of the discriminator threshold

A.4. Scintillator Assemblies: Adjusting Coincidences
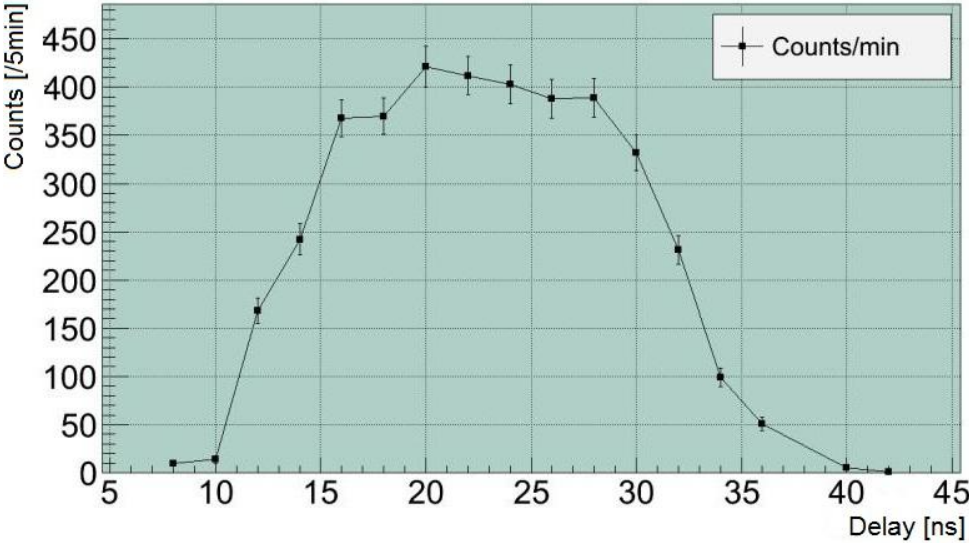
Figure A.7: The coincidence curve for the lower level: the number of coincidences as a function of the delay between the scintillators of the lower level

A.5. Drift Velocity for Different Mixtures of Argon-Carbon Dioxide
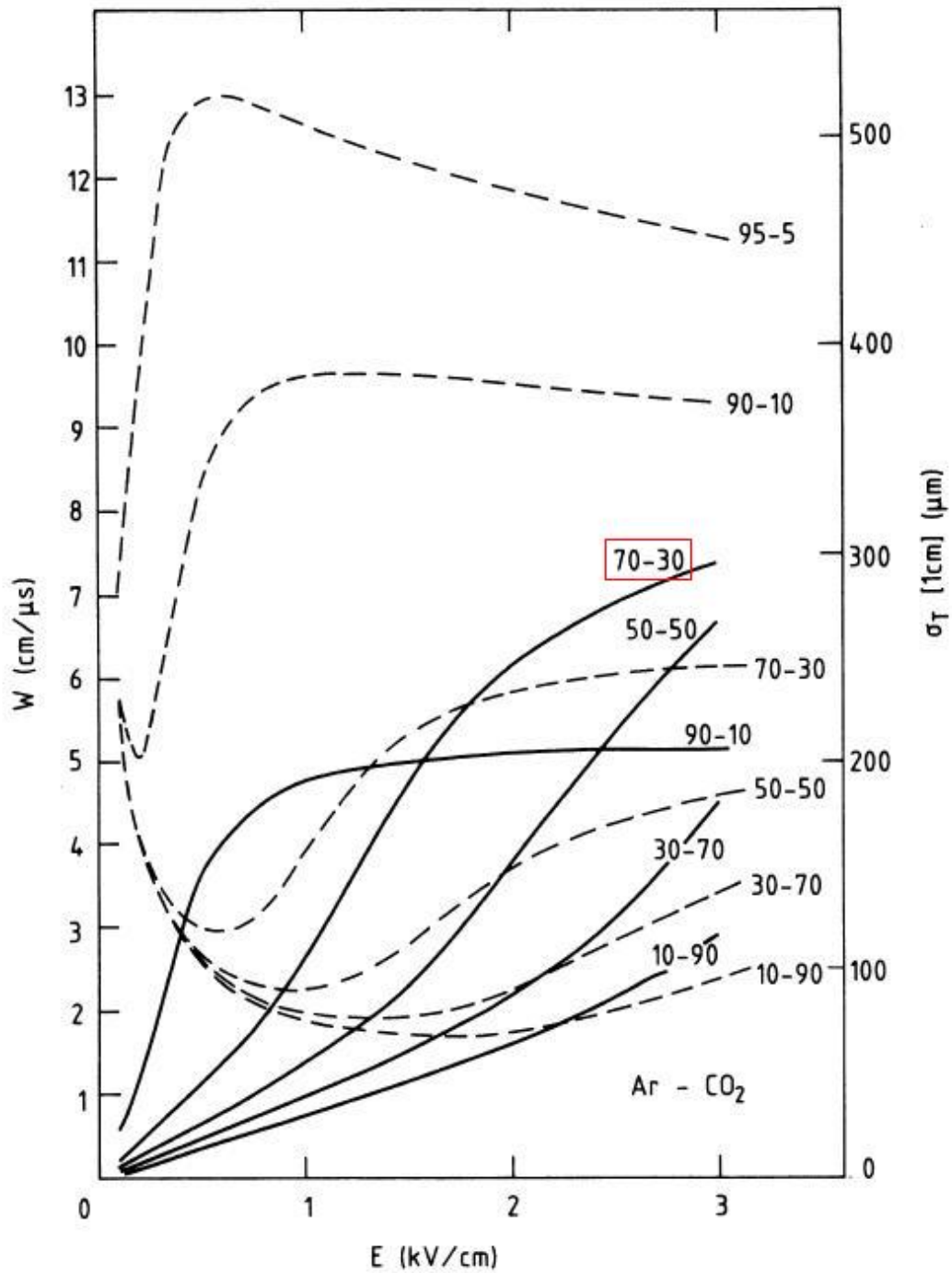
Figure A.8: Drift velocities w (cm/μs) (solid line) and transversal diffusion for 1 cm drift σ_T [1cm] (μm) (dashed line) as a function of drift field E (kV/cm) for different mixtures of Argon-Carbondioxide at normal pressure [21]

References

[1] Rudolph LEY, PS Division, CERN, 02.09.96.

[2] ALICE Collaboration. "ALICE TRD Technical Design Report". Technical Report CERN/LHCC 2001-021, CERN, 2001.

[3] ALICE Collaboration. E. Scomparin, "ALICE Results on Quarkonia", (2012), arXiv:1211.1623v1 [nucl-ex].

[4] K. Yagi et al.: "Quark-Gluon Plasma", Cambridge University Press, (2005).

[5] ALICE Collaboration. F. Carminate et al., "ALICE Physics Performance Report, Volume I", J. Phys. G: Nucl. Part. Phys. 30, 1517 (2004).

[6] ALICE Collaboration. "The ALICE Detector". URL http://aliceinfo.cern.ch/Public/en/Chapter2/Chap2Experiment-en.html FROM: 11.03.2012.

[7] C. Grupen and B. A. Schwartz: "Particle Detectors", 2nd ed. Cambridge: Cambride University Press (2008).

[8] K. Kleinknecht: "Detektoren für Teilchenstrahlung", 4. Aufl. Stuttgart: Teubner (2005).

[9] J. Beringer, *et al. (Particle Data Group)*, Phys. Rev. D86, 010001 (2012).

[10] W. Sommer, Ph.D Thesis, unpublished, "Measurements of Quarkonia with central detectors of ALICE", Goethe Universitt Frankfurt am Main, (2008).

[11] W. Leo: "Techniques for Nuclear and Particle Physics Experiments", Heidelberg: Springer (1987).

[12] C. Grupen: "Astroteilchenphysik", Braunschweig: Vieweg (2000).

[13] R. Diehl, "Particle Acceleration in Cosmic Sites", The European Physics Journal D 55: 509-518, (2009).

[14] M. Hoppe, Diploma Thesis, "Aufbau und Inbetriebnahme einer Funkenkammer", Westfälische Wilhelms-Universität, Institut für Kernphysik, (2004).

[15] Biermann, P. and Sigl, G.: "Introduction to Cosmic Rays", astro-ph/0202425.

[16] Demtroeder, W.: "Experimentalphysik 4: Kern-, Teilchen- und Astrophysik", Heidelberg: Springer (2010).

[17] Rainer Schicker, private communication.

[18] Sauli, F., "Principle of Operation of Multiwire Proportional and Drift Chambers", Cern 77-09 (1976).

[19] The ALICE Collaboration, R. Veenhof, "Choosing a Gas Mixture for the ALICE TPC", ALICE-INT-2003-29 (2003).

[20] ROOT. URL http://root.cern.ch.

[21] Sauli, F. and Preisert A., "Drift and Diffusion of Electrons in Gases: A Compilation", Cern 84-08 (1984).

[22] A. Andronic et al., "Pulse Height Measurements and Electron Attachment in Drift Chambers Operated with Xe, CO2 mixtures", (2003), arXiv:physics/0303059v1 [physics.ins-det].

[23] P. Braun-Munziger, K. Redlich, J. Stachel, "Particle Production in Heavy Ion Collisions", nucl-th/0304013, (2003).

[24] A. Andronic *et al.*, "Drift Velocity and Gain in Argon- and Xenon- Based Mixtures", Nucl.Inst.Meth., A523 (2003) 302.

Acknowledgements

First of all, I would like to thank Dr. Kai Schweda for the opportunity and his encouragement to work in the interesting field of nuclear and detector physics. His experience helped me along in working on this thesis project.

I especially want to thank Jochen Klein for his support I received within the work of my thesis.

Furthermore I would like to thank Dr. Yvonne Pachmayer for her support concerning all questions and issues on the commissioning of the prototype TRD chamber. I am also indebted to Ingo Deppner for helping me to set up the trigger set-up and the gas supply. I would also like to thank Dr. Rainer Schicker for his support in questions about the gas supply system. I also want to thank Dr. Anton Andronic giving me the opportunity to work with a TRD chamber.

My gratitude also goes to the the members of the Electronics Workshop, Dr. Venelin Angelov, Frank Schumacher and Klaus Layer. I would like to thank Dr. Bernd Windelband, Stefan Hetzel and Andrea Anjam from the Mechanical Workshop.

I would also like to thank the members of the ALICE group at the Phyisikalisches Institut at the University of Heidelberg. Special thanks goes to Prof. Dr Johanna Stachel, Prof. Dr. Peter Glaessel, Dr. Oliver Busch, Johannes Stiller, Michael Winn, Daniel Lohner, Dr. Min Jung Kweon, Dr. Jorge Mercado and Felix Reidt.

I would like to thank my parents and my brother for more than could possibly be expressed here.

Erklärung

Ich erkläre, dass ich die Arbeit selbstständig angefertigt und nur die angegebenen Hilfsmittel benutzt habe. Alle Stellen, die dem Wortlaut oder dem Sinn nach anderen Werken, gegebenfalls auch elektronischen Medien, entnommen sind, sind von mir durch Angabe der Quelle als Entlehnung kenntlich gemacht. Entlehungen aus dem Internet sind durch Ausdruck belegt.